



Selective synthesis of olefins via CO₂ hydrogenation over transition-metal-doped iron-based catalysts

Haiyan Yang^{a,b,1}, Yaru Dang^{a,c,1}, Xu Cui^a, Xianni Bu^a, Jiong Li^d, Shenggang Li^{a,b,*},
Yuhan Sun^a, Peng Gao^{a,b,*}

^a CAS Key Laboratory of Low-Carbon Conversion Science and Engineering, Shanghai Advanced Research Institute, Chinese Academy of Sciences, Shanghai 201210, China

^b University of Chinese Academy of Sciences, Beijing 100049, China

^c Hebei Normal University of Science & Technology, Qinhuangdao 066004, China

^d Shanghai Synchrotron Radiation Facility, Zhangjiang National Lab, Shanghai Advanced Research Institute, Chinese Academy of Sciences, Shanghai 201204, China

ARTICLE INFO

Keywords:

Carbon dioxide hydrogenation
Modified Fischer-Tropsch synthesis
Olefins
Iron catalysts
Transition metal promoter

ABSTRACT

The catalytic hydrogenation of CO₂ to olefins has received considerable attention. Herein, transition metal- and sodium-modulated iron-based catalysts were fabricated. Doping with zinc and copper favor the formation of Fe₃O₄ and Fe₅C₂ active phases, while adding manganese inhibits the formation of iron carbide. In addition, phase separation between copper and iron species occurs more readily under working conditions. Therefore, a zinc- and sodium-modulated Fe catalyst exhibited the best activity and stability. Moreover, copper was predicted to substantially decrease the energy barrier of the rate-determining step for the secondary hydrogenation of olefins and result in a much lower olefin-to-paraffin ratio. In addition, the ZnO/Fe₅C₂ interface facilitated the desorption of olefins from the catalyst surface and inhibited the undesirable secondary reaction of olefins, enabling a high selectivity toward olefins of 36.9 % C₂₋₄ and 32.3 % C₅₊. This study provides an exemplary new strategy for tuning the product selectivity of catalysts for olefin synthesis.

1. Introduction

The rapid increase in carbon-based energy consumption alongside the development of the global economy is responsible for high carbon dioxide (CO₂) emissions, which lead to severe environmental issues [1, 2]. To mitigate the excessive emissions of CO₂ and to also reduce reliance on fossil fuels, alternative routes for producing value-added chemicals and carbon-neutral fuels from captured CO₂ with the aid of renewable hydrogen (H₂) have received wide interest [3–7]. The direct hydrogenation of CO₂ to value-added C₂₊ hydrocarbons, for example, olefins, aromatics, and gasoline, has gained great attention. Among them, olefins, traditionally obtained from fossil resources, are valuable building blocks for producing industrially important compounds. Light olefins (C₂₋₄) are gateway molecules in the chemical industry, while heavy olefins (C₅₊) act as pivotal materials in the production of polymers, alcohols, lubricants, and detergents [8,9].

However, it is still a grand challenge to simultaneously achieve high

CO₂ conversion and high selectivity of C₂₊ hydrocarbons due to the chemical inertness of CO₂ and poor activity toward the subsequent chain propagation. Moreover, the produced olefins with unsaturated C=C bonds might be further hydrogenated into saturated paraffins, thus reducing their economic values. In recent years, alkali metals such as sodium (Na) or potassium (K) modified iron (Fe) catalysts have been extensively studied due to their intrinsic activity in both the reverse water gas shift (RWGS) reaction and the Fischer-Tropsch synthesis (FTS) process at a relatively high reaction temperature (>300 °C) [10]. It has been shown that Na or K plays an essential role in the selective formation of olefins, as it not only enhances the basicity of the catalyst required for CO₂/CO adsorption and suppresses the activation of H₂, but also promotes the formation of iron carbide that is required for olefin formation [11–16].

Nevertheless, the relatively high reaction temperature of the process weakens the chain growth reaction, and light olefins are usually obtained over these iron-based catalysts with poor stability [14,17–23].

* Corresponding authors at: CAS Key Laboratory of Low-Carbon Conversion Science and Engineering, Shanghai Advanced Research Institute, Chinese Academy of Sciences, Shanghai 201210, China.

E-mail addresses: lsg@sari.ac.cn (S. Li), gaopeng@sari.ac.cn (P. Gao).

¹ These authors contributed equally.

Attempts to enhance the carbon chain growth and durability of iron-based catalysts have involved doping the catalysts with transition metals, such as zinc (Zn), copper (Cu), manganese (Mn) and cobalt (Co) [14,24–31]. Among them, Zn has been the most widely investigated in Fe-based catalysts, where the strong interaction between Zn and Fe in the resulting lattice spinel structure increases surface basicity, thus increasing the carbon monoxide (CO) adsorption capacity and preventing Fe sintering [12,23–25]. It has been revealed that the addition of Cu lowers the chain growth probability, resulting in high selectivity of light olefins by favoring H-assisted CO dissociation [19]. However, the presence of Cu in CuFeO_2 catalysts was reported by Choi et al. to enhance the reduction and carburization of Fe species, consequently promoting chain growth with a C_{5+} selectivity of approximately 65 % [32]. Similarly, it was found by Liu et al. that when the Cu was added into iron-based supported catalysts, the selectivity of C_{2-4}^- decreased while the C_{5+} selectivity increased due to the strong interaction between Cu and Fe [33]. In addition, it was demonstrated that the interfacial sites between Cu and iron carbides contribute to efficient C–C coupling into long-chain olefins [34]. Mn is widely used as a promoter, and electron transfer from Mn to Fe species has been shown to facilitate the dissociative adsorption of CO and weaken its hydrogenation activity, thus favoring C–C coupling [14,26]. Nevertheless, it has also been shown that the addition of Mn facilitates the formation of Fe_5C_2 and decreases the adsorption of CO, resulting in the weakening of carbon chain growth [20]. Considering that the promoting effect of Co has been extensively studied and that Co is also an FTS active site, Co is not considered in the present work [24,27,35–37]. Therefore, the complexity of Fe-based catalysts makes this research very challenging, and the role of transition-metal modifiers remains controversial. Moreover, previously published works have mainly focused on the synthesis of light olefins [32,38–40], with few investigations on the role that transition-metal promoters have on the performance of the full spectrum of olefin products. Furthermore, there is also a lack of theoretical understanding of the effect that these transition-metal promoters have on olefin selectivity. Therefore, these severely limit our ability in rationally designing better iron-based catalysts for producing olefins.

Herein, we report transition metals (Zn, Cu, Mn) and Na decorated iron catalysts for CO_2 hydrogenation to olefins. By combining various *in*- and *ex-situ* characterization techniques along with density functional theory (DFT) calculations, the promoting effects that the transition metal promoters have on the Fe-based catalysts were elucidated. In particular, an iron catalyst featuring Zn and Na was found to exhibit outstanding activity ($33.2 \text{ mmol CO}_2 \text{ g}_{\text{Fe}}^{-1} \text{ h}^{-1}$) and the highest overall selectivity towards olefins (69.2 %) with the proportions of C_{2-4}^- and C_{5+} being 36.9 % and 32.3 %, respectively.

2. Experimental and computational methods

2.1. Catalyst preparation

The transition metals promoted iron-based catalysts were fabricated by a co-precipitation method. In a typical preparation, 500 mL NaOH solution (1.5 mol L^{-1}) was added dropwise into 150 mL aqueous solution containing 0.12 mol of $\text{Fe}(\text{NO}_3)_3 \cdot 9\text{H}_2\text{O}$ and 0.04 mol of $\text{M}(\text{NO}_3)_x$ ($\text{M} = \text{Zn, Cu or Mn}$) under vigorous stirring at 60°C until the pH value reached around 9. Afterwards, the obtained slurry was aged for 1 h, and washed with deionized water to control the residual content of Na. Subsequently, the filtered cakes were dried at 80°C overnight, and calcined at 400°C for 3 h. The as-prepared catalysts were denoted as FeZn-Na, FeCu-Na and FeMn-Na. For comparison, Fe-Na catalysts was also synthesized by the same procedure but without the addition of $\text{M}(\text{NO}_3)_x$.

2.2. Catalyst characterization

Chemical components of the as-prepared catalysts were determined on an inductively coupled plasma optical emission spectrometer (ICP-

OES) after digested according to the standard in-house procedures.

X-ray diffraction (XRD) measurements were conducted on a Rigaku Ultima IV diffractometer with the $\text{Cu K}\alpha$ radiation. For the *in situ* XRD experiment, the catalysts were exposed to pure H_2 and the patterns were recorded at $30\text{--}700^\circ\text{C}$.

The Brunauer-Emmett-Teller (BET) specific surface areas and Barrett-Joyner-Halenda (BJH) pore volumes of the catalysts were determined using a TriStar II 3020 instrument.

The micromorphology and nanostructure of the catalysts were studied on a high-resolution transmission electron microscope (HRTEM, Tecnai G220) and a scanning electron microscope (SEM, SUPRRATM 55).

H_2 temperature-programmed reduction (H_2 -TPR) were performed on a Micromeritics ChemiSorb 2920. The reduction carburization behaviors of the catalysts were investigated by CO temperature-programmed reduction (CO-TPR) in the same apparatus connected to an online mass spectrometer (MS, Pfeiffer OmniStar GSD320 02) for analyzing the outlet gases for CO and CO_2 . For each trial, 50 mg catalyst was used and pretreated in pure Ar at 150°C for 2 h. The measurement was taken from 50 to 750°C at $10^\circ\text{C min}^{-1}$ in 5 % H_2/Ar for H_2 -TPR or 5 % CO/Ar for CO-TPR.

CO_2 temperature-programmed desorption (CO_2 -TPD) experiments were also carried out on the Micromeritics ChemiSorb 2920 connected to an MS. Firstly, 100 mg catalysts were pretreated in pure Ar at 150°C for 2 h, and then cooled down to 50°C . After saturated with CO_2 for 0.5 h, the system was flushed with Ar. Finally, the measurement was taken from 50 to 750°C at $10^\circ\text{C min}^{-1}$ under Ar atmosphere.

H_2 temperature-programmed desorption (H_2 -TPD) measurements were carried out on the same apparatus as CO_2 -TPD. Firstly, 100 mg catalysts after reaction for 40 h were pretreated at 350°C for 2 h with pure Ar, and then cooled down to 50°C . Subsequently, the system was saturation with H_2 for 0.5 h, and then flushed with Ar. Finally, the measurement was taken from 50 to 750°C at $10^\circ\text{C min}^{-1}$ in Ar atmosphere to monitor the desorption of H_2 .

X-ray photoelectron spectroscopy (XPS) measurements were acquired on a Thermo Scientific K-Alpha spectrometer with the $\text{Al K}\alpha$ radiation. All binding energies were calibrated by reference signal of C 1 s at 284.8 eV .

C_3H_6 pulse transient hydrogenation (C_3H_6 -PTH) experiments were conducted on a self-made fixed-bed reactor. In brief, 40.0 mg catalyst was *in situ* activated in H_2 at 350°C for 8 h. Then, a reactant gas mixture (73 % H_2 , 24 % CO_2 , 3 % N_2) was switched on at 320°C and 3 MPa. After 40 h reaction, the pressure was reduced to the atmospheric pressure and the feed gas was switched back to pure H_2 . Afterwards, 0.5 mL of diluted C_3H_6 (7.5 % $\text{C}_3\text{H}_6/\text{Ar}$) was pulsed into the reactor in a time interval of 5 min, while signals at the m/z values of 41 (C_3H_6) and 43 (C_3H_8) were recorded by the MS.

Mössbauer spectroscopy were adopted to quantify the iron-containing phases on a Topologic 500 A spectrometer using the ^{57}Co (Rh) radioactive source.

The X-ray absorption spectroscopy (XAS) experiments were conducted on the BL11B beamline of Shanghai Synchrotron Radiation Facility.

2.3. Catalytic performance evaluation

CO_2 hydrogenation to olefins were performed on a fixed-bed reactor. Typically, 1.5 g catalyst diluted with 3.0 g quartz sand (both in 40–60 mesh) was placed in a stainless tube reactor. Prior to the reaction, the catalyst was *in situ* activated with pure H_2 (100 mL min^{-1}) at 350°C for 8 h under atmospheric pressure. After cooling down to 150°C , the reactant gas mixture (73 % H_2 , 24 % CO_2 , 3 % N_2) was introduced to the reactor, followed by the increase of the temperature and pressure to the standard reaction conditions of 320°C , 3 MPa, $4000 \text{ mL g}_{\text{cat}}^{-1} \text{ h}^{-1}$.

The gaseous effluents were quantitatively analyzed using an online gas chromatography (GC, Shimadzu GC-2010 C). Typically, H_2 , N_2 , CO,

CH₄, and CO₂ were analyzed by a GC with a thermal conductivity detector (TCD). Hydrocarbons were detected by another GC equipped with a flame ionization detector (FID). The liquid products were acquired in a cold trap and analyzed offline using the GC. Product selectivity was calculated based on the carbon balance. As the total selectivity of oxygenates (mainly alcohols) was below 5.0 %, they were not further considered in this study. After quantifying all other products, the carbon balance for each test exceeded 95.0 %.

CO₂ conversion (X_{CO_2}) was calculated using an internal normalization method according to Eq. (1):

$$X_{\text{CO}_2} = \frac{CO_{2\text{inlet}} - CO_{2\text{outlet}}}{CO_{2\text{inlet}}} \times 100\% \quad (1)$$

CO selectivity (S_{CO}) was calculated from Eq. (2):

$$S_{\text{CO}} = \frac{CO_{\text{outlet}}}{CO_{2\text{inlet}} - CO_{2\text{outlet}}} \times 100\% \quad (2)$$

Distribution of the hydrocarbons was obtained according to Eq. (3):

$$S_{C_iH_j} = \frac{C_iH_j \times i}{\sum_{i=1}^n C_iH_j \times i} \times 100\% \quad (3)$$

Space time yield of olefins (STY_{olefins} , $\text{mg g}_{\text{cat}}^{-1} \text{h}^{-1}$) was obtained according to Eq. (4):

$$STY_{\text{olefins}} = \frac{F_{\text{CO}_2} \times X_{\text{CO}_2} \times (1 - S_{\text{CO}}) \times S_{\text{olefins}} \times 14 \times 1000}{m_{\text{cat}}} \quad (4)$$

The Activity ($\text{mmol g}_{\text{Fe}}^{-1} \text{h}^{-1}$), which is defined as the CO₂ conversion rate per gram of Fe, was calculated from Eq. (5):

$$\text{Activity} = \frac{F_{\text{CO}_2} \times X'_{\text{CO}_2} \times 1000}{m_{\text{Fe}}} \quad (5)$$

where $CO_{2\text{inlet}}$ and $CO_{2\text{outlet}}$ refer to moles of CO₂ at the inlet and outlet, respectively; CO_{outlet} represents moles of CO at the outlet; C_iH_j is moles of the hydrocarbon with a carbon number i at the outlet; F_{CO_2} represents the molar flow rate of inlet CO₂; S_{olefins} represents the selectivity of olefins in hydrocarbons obtained according to Eq. (4), and m_{cat} represents the weight of the catalyst used; X'_{CO_2} represents the maximum CO₂ conversion, m_{Fe} represents the weight of the Fe used.

2.4. DFT calculations

Periodic density functional theory (DFT) calculations were carried out with the Vienna ab initio simulation package (VASP) [41]. The Perdew-Burke-Ernzerhof (GGA-PBE) functional was used to calculate the electron exchange and correlation energies in the generalized gradient approximation [42]. The projector-augmented wave (PAW) method was used to describe the electron-ion interactions [43]. Electron smearing was enabled via the Methfessel-Paxton method with the smearing width of $\sigma = 0.2$ eV. An energy cutoff of 400 eV and a force convergence of 0.05 eV/Å were employed.

The Fe₅C₂ primitive unit cell is monoclinic with the C2/c crystallographic symmetry. The calculated lattice parameters ($a = 11.543$ Å, $b = 4.494$ Å, $c = 4.981$ Å, and $\beta = 97.60^\circ$) are in reasonable agreement with the experimental values ($a = 11.562$ Å, $b = 4.573$ Å, $c = 5.060$ Å and $\beta = 97.74^\circ$). The $p(2 \times 2)$ supercell of the Fe₅C₂(111) slab was employed to model the pure Fe₅C₂(111) surface, and also to build the structures of the Cu/Fe₅C₂(111) and ZnO/Fe₅C₂(111) interfaces, which were sampled with the $(3 \times 3 \times 1)$ k-point grid in the DFT calculations. More specifically, the Fe₅C₂(111) slab model includes 48 C and 96 Fe atoms, of which 16 C and 40 Fe atoms at the slab bottom were fixed. Furthermore, 8 Cu atoms were added to obtain the Cu/Fe₅C₂(111) interfacial model, and 8 Zn and 6 O atoms were added to result in the ZnO/Fe₅C₂(111) interfacial model. To avoid possible interactions between adjacent slabs, a vacuum spacing of 20 Å was inserted. The climbing image nudged

elastic band (CI-NEB) method with usually 5 images was used to located the transition states [44]. The VESTA program was used to analyse the charge transfer between adsorbate and surface by calculating the charge difference before and after the adsorption of an adsorbate [44]. In addition, Bader atomic charge analysis was performed to estimate the number of electrons transferred from the Cu or ZnO component to the Fe₅C₂(111) surface [44].

3. Results and discussion

3.1. Composition and structural properties of Fe-based catalysts

FeZn-Na, FeCu-Na and FeMn-Na catalysts were synthesized via a co-precipitation method, with an Fe-Na catalyst also prepared for comparison. By controlling the washing times, all the catalysts had similar residue Na content (around 2.5 wt%), as determined by ICP-OES (Table S1), and the molar ratio of Fe:M (M = Zn, Cu, or Mn) was close to 3 for the modified catalysts.

The catalysts exhibit a characteristic mesoporous structure, as evidenced by their hysteresis loops at a relative pressure (P/P_0) of 0.5–1.0 with the average pore size centered at 10–20 nm (Fig. S1). Compared with Fe-Na, the incorporation of transition metals decreased the pore size of the iron catalysts to 17.2, 13.2, and 11.0 nm for FeCu-Na, FeMn-Na and FeZn-Na, respectively. The introduction of Mn increased the BET specific surface area and pore volume from 62 $\text{m}^2 \text{g}^{-1}$ and 0.155 $\text{cm}^3 \text{g}^{-1}$ for Fe-Na to 72 $\text{m}^2 \text{g}^{-1}$ and 0.226 $\text{cm}^3 \text{g}^{-1}$ for FeMn-Na, respectively, while the Zn and Cu as promoters decreased the surface area and pore volume.

XRD patterns of the calcined catalysts are shown in Fig. 1a. The Na was well distributed in all the catalysts, as confirmed by the absence of diffraction peaks associated with Na species. Pristine Fe-Na and FeMn-Na catalysts exhibited a typical hematite phase of $\alpha\text{-Fe}_2\text{O}_3$ (JCPDS, 33-0664); the dominant crystalline phase of ZnFe₂O₄ (JCPDS, 22-1012) was observed for FeZn-Na; and the pristine FeCu-Na consisted of $\alpha\text{-Fe}_2\text{O}_3$ and CuO (JCPDS, 48-1548). The absence of diffraction peaks associated with the MnO_x phase indicated that Mn was highly dispersed in the $\alpha\text{-Fe}_2\text{O}_3$ bulk matrix, concomitant with an increase in the specific surface area of iron oxides after the addition of Mn. The crystallite sizes of the iron species calculated using the Scherrer equation are listed in Table S1. Zn and Mn decreased the crystal size of the iron species from 17.1 nm for Fe-Na to 13.7 nm and 13.5 nm for FeZn-Na and FeMn-Na, respectively. However, the average crystalline size of FeCu-Na was 21.4 nm, much larger than those of the other catalysts.

The morphologies of fresh catalysts were investigated using TEM, with results shown in Fig. 2 and Fig. S2. Fe-Na was found to be well dispersed as rod-like nanoparticles with a length of around 17.7 nm. In terms of FeZn-Na, spherical nanoparticles with a smaller diameter of 13.8 nm were observed due to the formation of spinel ZnFe₂O₄. The rough size of FeCu-Na was 4–31 nm, and the larger nanoparticles could be ascribed to Fe₂O₃, while the particles with a size of approximately 6 nm could be assigned to CuO. In the case of FeMn-Na, the main phase was Fe₂O₃, which consisted of much smaller nanoparticles with a mean size of 10.3 nm. EDX mapping was conducted to investigate the elemental distribution of the pristine catalysts. As presented in Table S1 and Fig. S3, Na is homogeneously distributed, and the Na content of all the catalysts is about 2.6–2.7 wt%, consistent with the ICP-OES results. In addition, the Fe-Na, FeZn-Na, and FeMn-Na all showed uniform distributions of Fe and the other transition metal (i.e. Zn or Mn). However, Cu agglomeration was observed for the FeCu-Na, which provided evidence of a phase separation between Fe and Cu. Based on the above results, it was concluded that the addition of Zn and Mn significantly enhanced the dispersion of Fe species and decreased the particle size of the iron phase.

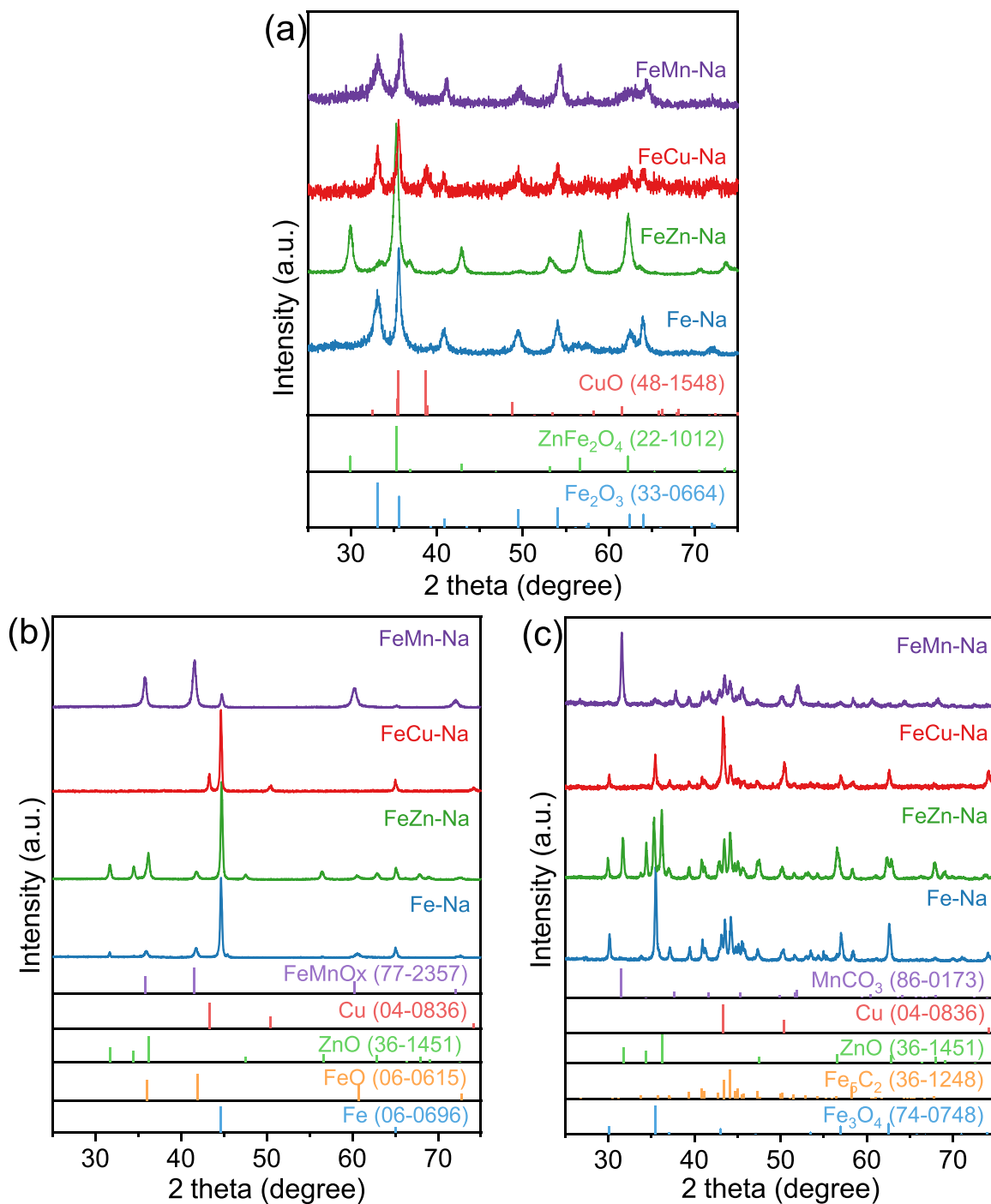


Fig. 1. XRD patterns of the Fe-based catalysts after (a) calcination, (b) reduction, and (c) reaction for 40 h.

3.2. Phase transformation during activation

The catalysts were activated under a flow of H_2 prior to the evaluation. After reduction at $350\text{ }^\circ\text{C}$ for 8 h, in the XRD data of the activated Fe-Na catalyst the diffraction peaks (Fig. 1b) of Fe_2O_3 disappeared, while peaks corresponding to α -Fe (JCPDS, 06-0696) and FeO (JCPDS, 06-0615) appeared. For the activated FeZn-Na catalyst, the diffraction peaks belonging to $ZnFe_2O_4$ were negligible and those assigned to α -Fe, FeO and ZnO (JCPDS, 36-1451) were visible. Apart from the observation of α -Fe, metallic Cu was also found to be present in the reduced FeCu-Na, as displayed by the peaks observed at 43.3° and 50.4° (JCPDS, 04-0836). It is noteworthy that there were no characteristic peaks associated with FeO for FeCu-Na, implying that the addition of Cu promoted the

reduction of Fe species. Unlike the other catalysts, the activated FeMn-Na catalyst was found to consist of a mixed phase of α -Fe and $FeMnO_x$ (JCPDS, 77-2357), with the presence of the latter suggesting close interaction between Fe and Mn.

The reduction process was also tracked using *in situ* XRD (Fig. 3). With increasing reduction temperature, the iron phase was transformed to Fe_3O_4 (JCPDS, 74-0748), FeO, and further to Fe for all the catalysts. The intensity of the diffractions of Fe_2O_3 , the dominant phase of the Fe-Na, became weaker and finally vanished when the temperature reached $400\text{ }^\circ\text{C}$. Meanwhile, Fe_3O_4 formed and its intensity weakened, while the diffractions corresponding to α -Fe became more intense with increasing temperature. Finally, the iron species were totally reduced to α -Fe at $700\text{ }^\circ\text{C}$. Compared with the reduction process of Fe-Na, the diffraction

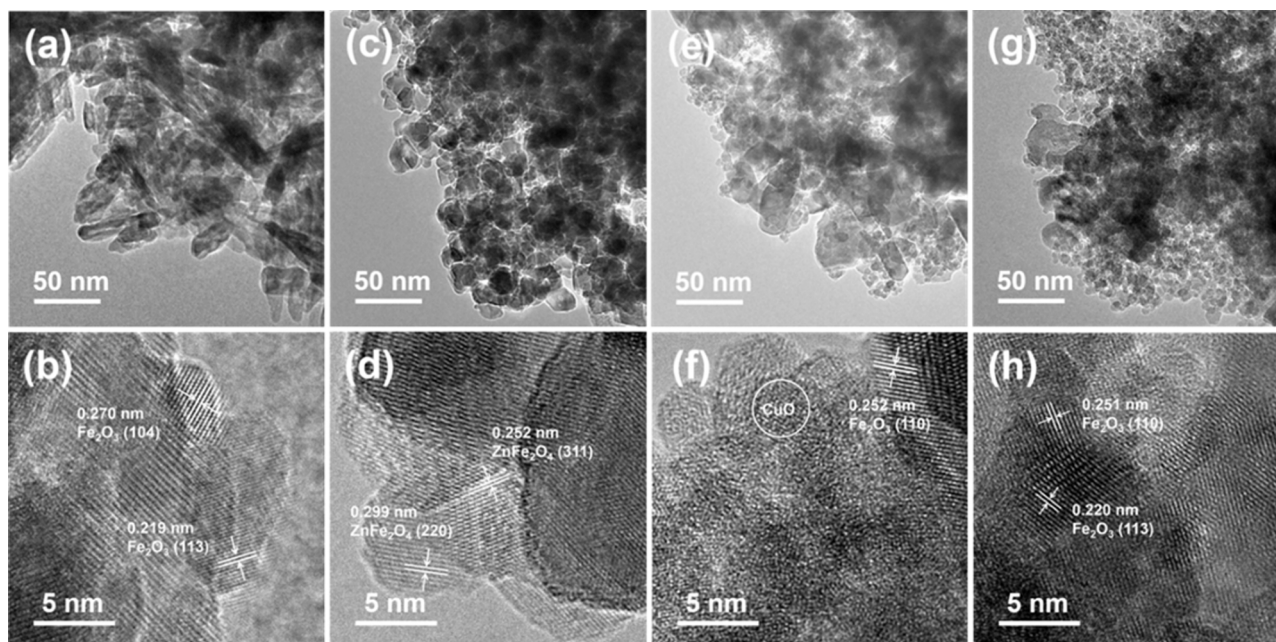


Fig. 2. TEM and HRTEM images of the Fe-based catalysts. (a, b) Fe-Na, (c, d) FeZn-Na, (e, f) FeCu-Na, and (g, h) FeMn-Na.

peaks corresponding to Fe_3O_4 , FeO , and $\alpha\text{-Fe}$ of the FeZn-Na appeared at much lower temperatures of 300, 450, and 450 °C, respectively, indicating that the introduction of Zn was beneficial for the reduction of iron species. For the FeCu-Na catalyst, CuO and Fe_2O_3 were reduced to Cu and Fe_3O_4 at 250 °C, respectively, and peaks associated with $\alpha\text{-Fe}$ arose at 350 °C, at a much lower temperature than those of the FeZn-Na catalyst, suggesting that the presence of Cu was more conducive to the reduction of the iron phase than the zinc species. The FeMn-Na catalyst exhibited a similar reduction process to that of FeZn-Na, whereas the diffraction peaks of Fe_3O_4 , FeMnO_x , and $\alpha\text{-Fe}$ appeared at a much lower temperature than those of Fe-Na. Moreover, MnO (JCPDS, 78-0424) did not form until the temperature reached 700 °C, further indicating the strong interaction between Mn and Fe species.

H_2 -TPR measurements were conducted to assess the promoting effect that the transition metals have on the reducibility of the Fe-based catalysts. As displayed in Fig. S4, several H_2 consumption peaks were observed for the Fe-Na catalyst, which reflected the stepwise reduction of the Fe_2O_3 to metallic Fe ($\text{Fe}_2\text{O}_3 \rightarrow \text{Fe}_3\text{O}_4 \rightarrow \text{FeO} \rightarrow \text{Fe}$). Combined with the in-situ XRD results (Fig. 3a), the peaks present in the range of 200–400 °C were assigned to the reduction of Fe_2O_3 to Fe_3O_4 , while those present at around 400–700 °C were attributed to the sequential reduction of Fe_3O_4 to FeO and further to $\alpha\text{-Fe}$. The reduction process of FeZn-Na was similar to that of Fe-Na, and the reduction of Zn^{2+} did not occur at a temperature of < 700 °C. However, the reduction peak of FeZn-Na shifted toward a lower temperature, showing that zinc oxide improved the reduction behavior of the iron catalyst, which endowed the FeZn-Na catalyst with more exposed active sites. For the FeCu-Na, only two obvious reduction peaks were observed, and the first peak at the low temperature (<350 °C) corresponded to the reduction of CuO to Cu and Fe_2O_3 to Fe_3O_4 , while the peak at the high temperature (>360 °C) represented the final transformation of Fe_3O_4 into $\alpha\text{-Fe}$. Similarly, all of the peaks of FeCu-Na began at a relatively low temperature, indicating that the addition of Cu significantly enhanced the reducibility of iron oxides, consistent with the in-situ XRD results (Fig. 3c). H_2 was dissociatively adsorbed at the Cu site once it was formed at around 250 °C, which led to H spillover and the reduction of iron species at a lower temperature [24,45]. Mn also enhanced the reducibility of iron oxides, as evidenced by the shift in the first H_2 consumption peak for FeMn-Na, which also affirmed the intimate contact between the iron species and transition metals.

CO-TPR experiments were conducted to investigate the reduction and carburization processes of the catalysts under a CO atmosphere. The CO-TPR profiles of the Fe-Na, FeZn-Na, and FeCu-Na catalysts contain three main peaks (Fig. 4). The first peak at 210–234 °C could be attributed to the reduction of Fe_2O_3 to Fe_3O_4 or the spinel ZnFe_2O_4 to Fe_3O_4 , as the CO consumption equaled the amount of CO_2 formed. Compared with the Fe-Na and FeZn-Na catalysts, the integral area of the first peak of FeCu-Na was much larger, also demonstrating that the addition of Cu increased the extent of reduction. The second peak was assigned to both the reduction and carburization processes of Fe_3O_4 , since the consumption of CO gradually exceeded the production of CO_2 . For the third peak, the consumption of CO was much greater than the production of CO_2 , indicating that carburization of the catalysts occurred and that the Fe species were completely reduced. For FeMn-Na, the peak area of CO consumption at ~225 °C was larger than that of CO_2 production, which was ascribed to the formation of MnCO_3 , resulting in a decrease in the amount of CO_2 in the outlet gas. Additionally, the peak associated with the reduction and carburization processes of Fe_3O_4 appeared at a relatively higher temperature (390 °C) than those of the other three catalysts, indicating that the carburization process of the FeMn-Na catalyst was more difficult than those of the other catalysts. Consequently, Mn inhibited the interactions of iron species with CO due to the strong interaction between Mn and Fe, and the Fe species was partially covered by Mn. Importantly, the two carburization peaks of FeZn-Na shifted toward a lower temperature compared with those of Fe-Na, suggesting that the incorporation of Zn was beneficial to the formation of iron carbide.

3.3. Phase compositions of the spent catalysts

To investigate the structural evolution of the catalysts during CO_2 hydrogenation, the XRD patterns for the 40 h spent catalysts were collected. As shown in Fig. 1c, diffraction peaks assigned to Fe_3O_4 and $\chi\text{-Fe}_5\text{C}_2$ (JCPDS, 36-1248) were identified for all of the catalysts, consistent with the well-known “tandem mechanism”, in which the two active sites (Fe_3O_4 and $\chi\text{-Fe}_5\text{C}_2$) are responsible for the RWGS reaction and the subsequent hydrogenation of CO to produce olefins, respectively [13,46,47]. The ZnO phase was still visible in the spent FeZn-Na catalyst. For the spent FeCu-Na catalyst, the Cu remained in metallic form. In terms of the spent FeMn-Na catalyst, the diffraction peaks for MnCO_3

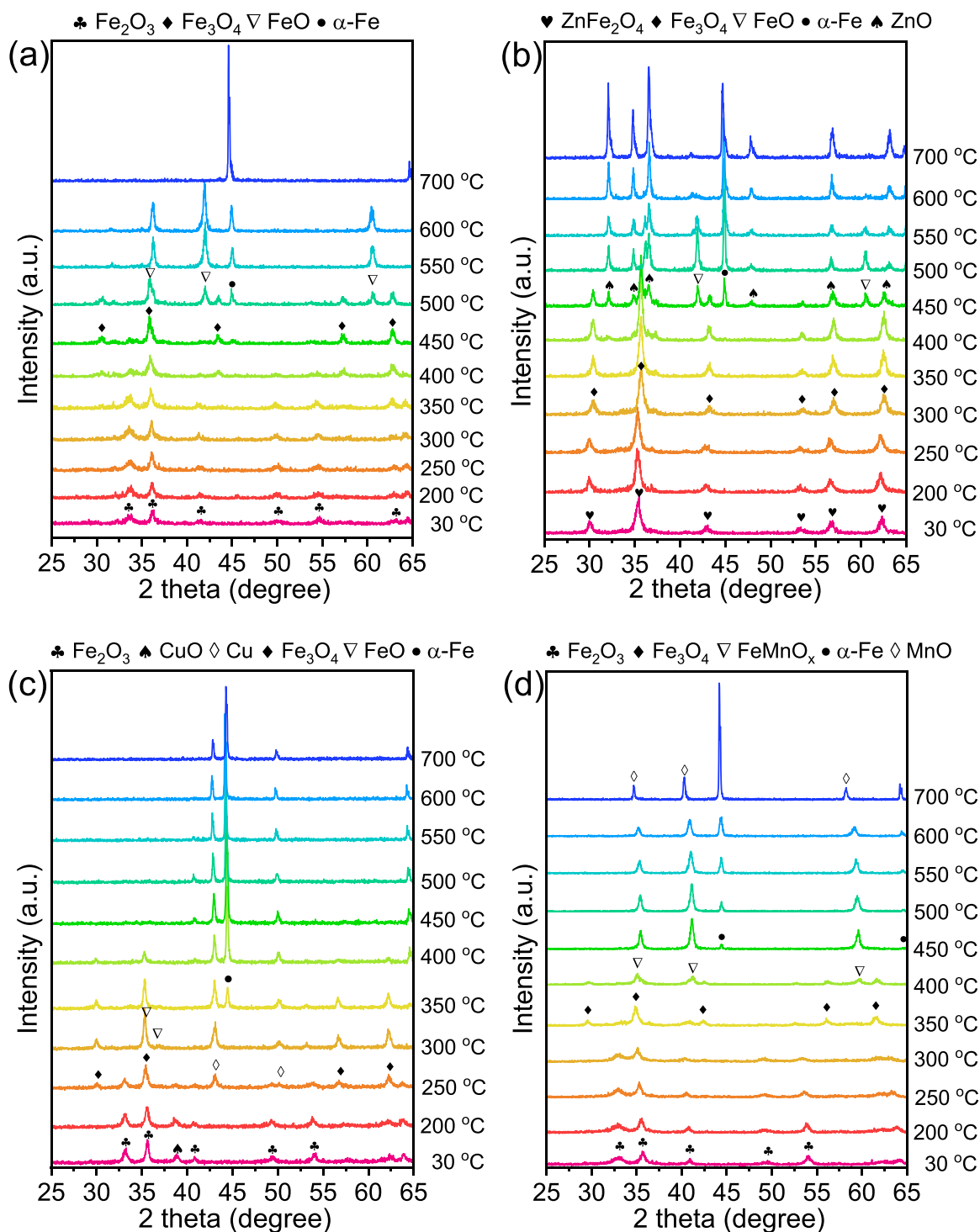


Fig. 3. In situ XRD patterns of the Fe-based catalysts. (a) Fe-Na, (b) FeZn-Na, (c) FeCu-Na, and (d) FeMn-Na.

(JCPDS, 86-0173) were detected mainly due to the reaction between CO₂ and MnO.

After reaction, the morphologies of the various catalysts showed obvious changes (Fig. 5 and Figs. S5–S7). Among them, the nanoparticle diameter of the Fe-Na catalyst increased significantly from 17.7 nm for the pristine sample to approximately 200 nm for the spent sample recovered after reaction for 40 h (Fig. S5), which suggested the remarkable agglomeration of the iron species during the reaction. The HRTEM images clearly showed the lattice fringes of Fe₃O₄ and Fe₅C₂ for all the catalysts, consistent with the above analysis. From the EDX

mapping of the spent FeZn-Na (Fig. 5), the Zn and Fe species were found to be in intimate contact with one another, as evidenced by the appearance of Fe in almost all regions where Zn was present. Similarly, the Fe and Mn species in the spent FeMn-Na catalyst were also in close contact with one another (Fig. S7). For the spent FeCu-Na catalyst, there was still a clear phase separation between Fe and Cu species (Fig. S6), and the distribution of Cu is more concentrated, which would inhibit the C–C coupling and decrease the selectivity toward long-chain hydrocarbons [34]. Moreover, it was found that Na and Zn were always distributed in the same region, indicating that Na was dispersed on the surface

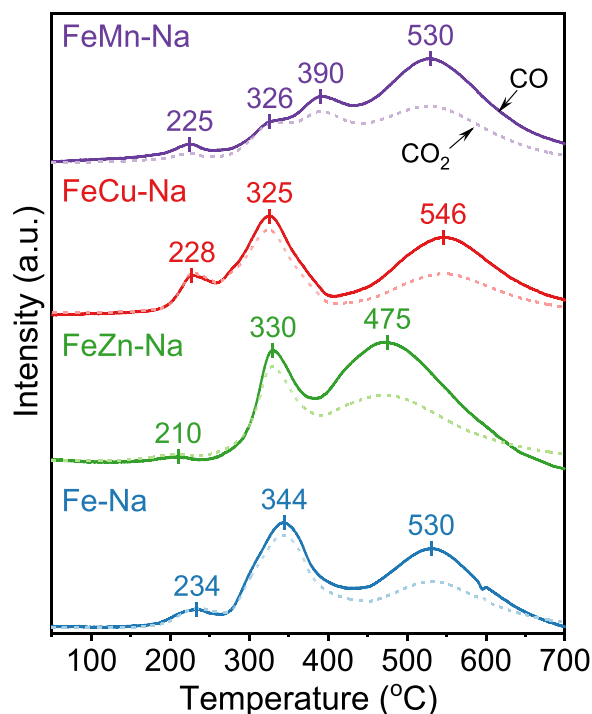


Fig. 4. The curves of CO consumption and CO₂ production during the CO-TPR process of the Fe-based catalysts.

of both the ZnO and Fe₅C₂ species.

To further study the nature of the active sites in the spent catalysts, XAS experiments were conducted, and the Fe K-edge X-ray absorption near-edge structure (XANES) spectra of the catalysts, as well as those of the Fe standards (Fe₃O₄ and Fe₅C₂), are shown in Fig. 6a. The chemical state of the spent FeMn-Na catalyst was similar to Fe₃O₄, while those of the other catalysts resembled Fe₅C₂. From the corresponding Fourier-transformed intensity of extended X-ray absorption fine structure (EXAFS) spectra (Fig. 6b), all of the spent catalysts exhibited predominant Fe–O (1.5 Å) and Fe–Fe (2.6 Å) scattering signals from the Fe₃O₄ phase, and the two major peaks at 1.6 Å and 2.2 Å could be ascribed to the Fe–C and Fe–Fe scatterings of Fe₅C₂, respectively. The XAS results thus further confirmed the presence of Fe₃O₄ and Fe₅C₂ phases in the activated Fe-based catalysts. Importantly, the distinct peak observed at 2.2 Å in the spectrum of the spent FeZn-Na was more intense than that of the other catalysts, implying that the introduction of zinc species induced a higher degree of carbide formation during the reaction, consistent with the CO-TPR results.

To quantify the active phases present during CO₂ hydrogenation, Mössbauer spectroscopy measurements were conducted (Fig. 7 and Table S2). After the reaction, the catalysts were comprised of two discernible active phases, namely Fe₃O₄ and χ -Fe₅C₂. The Mössbauer spectrum of the spent Fe-Na catalyst was fitted with one doublet and six sextets, where the doublet could be ascribed to the superparamagnetic phase of Fe²⁺/Fe³⁺ and the sextets with a hyperfine field (H_{hf}) of around 486 and 452 kOe were attributed to the tetrahedral and octahedral sites of Fe₃O₄, respectively [5]. Moreover, the sextets with H_{hf} values of around 215, 183, and 111 kOe were assigned to three different nonequivalent sites of χ -Fe₅C₂, which accounted for 63.5 %. Similarly, the dominant phase of the spent catalysts was χ -Fe₅C₂, with percentages of 76.4 %, 64.9 %, and 55.0 % for FeZn-Na, FeCu-Na, and FeMn-Na,

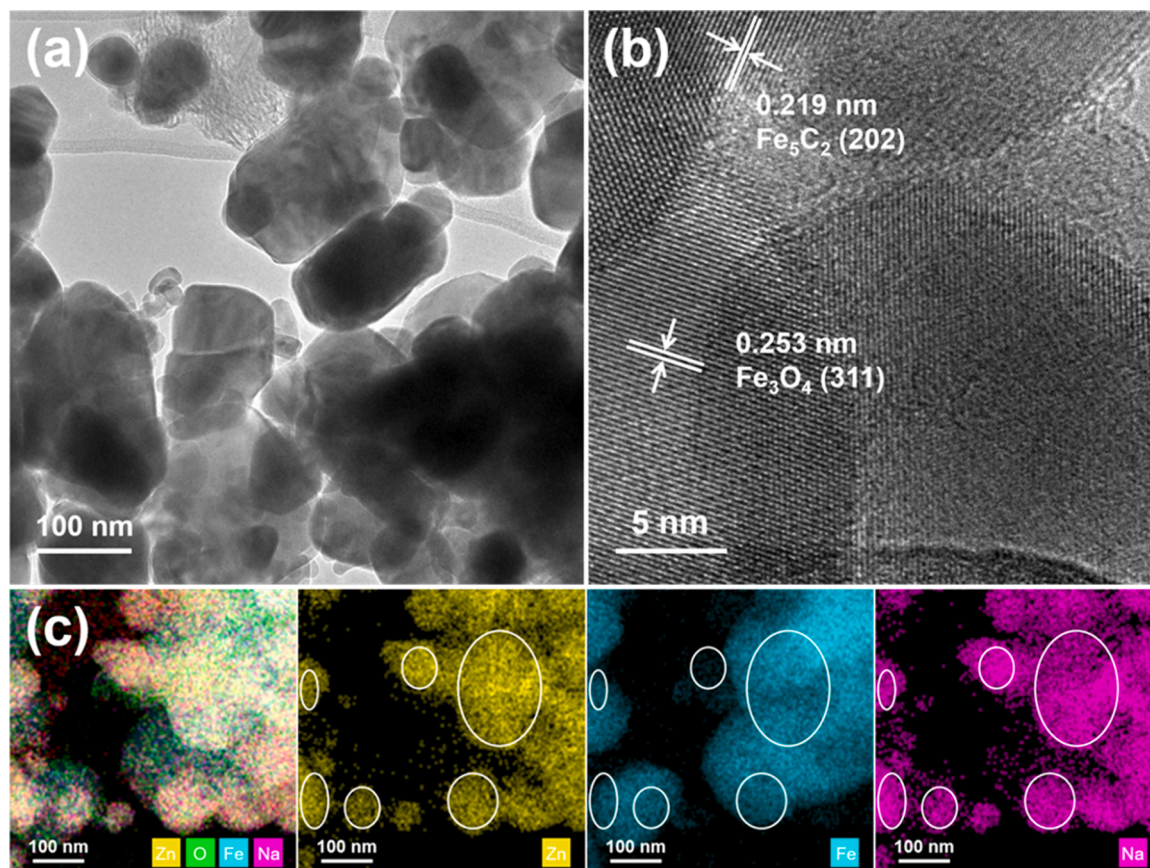


Fig. 5. (a) TEM, (b) HRTEM image, and (c) EDX elemental mapping of the spent FeZn-Na catalyst.

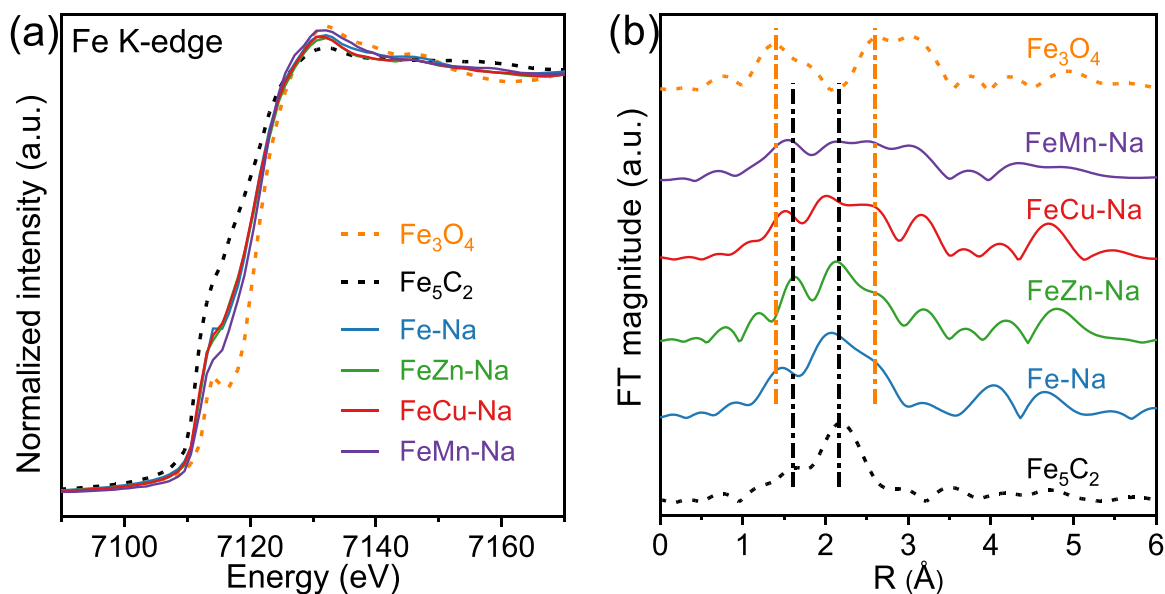


Fig. 6. (a) Fe K-edge XANES spectra and (b) the corresponding Fourier-transformed intensity of EXAFS spectra of the spent catalysts and Fe standards (Fe_3O_4 and Fe_5C_2).

respectively. Among them, the greater proportion of χ - Fe_5C_2 on the spent FeZn-Na catalyst was attributed to the promotion of the carburization of the iron species by the surface enrichment of Na, in addition to the strong ability of the Zn species to stabilize the χ - Fe_5C_2 [48]. In contrast, Mn hindered the carburization of Fe, and thus the spent FeMn-Na catalyst displayed the lowest proportion of Fe_5C_2 .

3.4. Surface chemistry of the Fe-based catalysts

A proper basicity of a catalyst is conducive to CO_2 adsorption and the subsequent C–C coupling. CO_2 -TPD experiments were thus conducted to investigate the surface basicity of the catalysts, with the results shown in Fig. 8a. The profiles were divided into three desorbed peaks, of which the α peak was assigned to the weak adsorption of CO_2 , while the β and γ peaks were associated with the desorption of CO_2 at medium-strength and strongly basic sites, respectively. The β and γ peaks shifted toward a higher temperature with the introduction of the transition metals into Fe-Na, confirming that these promoters enhanced the CO_2 adsorption strength of the catalyst. Besides this, the amount of CO_2 desorption was quantified and is summarized in Table S3. There were few medium-strength basic sites in the pristine Fe-Na catalyst. The amount of medium-strength basic sites increased with the addition of the transition metals, especially for the Zn and Cu promoters. The maximum amount of desorbed CO_2 of $14.7 \text{ mg g}_{\text{cat}}^{-1}$ was obtained over the FeCu-Na at medium-strength and strongly basic sites of 4.5 and $5.9 \text{ mg g}_{\text{cat}}^{-1}$, respectively, consistent with a previous study that suggested that Cu can act as an electron promoter to boost the surface basicity of catalysts [35].

It is known that the adsorbed H_2 on the catalyst surface can promote the RWGS reaction and subsequent transformation of the CO intermediates [5,49]. H_2 -TPD experiments were performed to analyze the activation of H_2 on the working catalysts, and the results are given in Fig. 8b and Table S3. It was found that the total amounts of H_2 desorbed from the spent FeZn-Na ($0.89 \text{ mg g}_{\text{cat}}^{-1}$) and FeCu-Na ($0.55 \text{ mg g}_{\text{cat}}^{-1}$) catalysts were much higher than for the Fe-Na ($0.34 \text{ mg g}_{\text{cat}}^{-1}$) catalyst, indicating that the addition of Zn and Cu remarkably enhanced the activation of H_2 , whereas Mn reduced the adsorption capacity of H_2 ($0.27 \text{ mg g}_{\text{cat}}^{-1}$). Thus, ZnO and Cu were effective in inducing H_2 spillover, which enhanced H_2 desorption over the FeZn-Na and FeCu-Na catalysts. In addition, the highest iron carbide content formed on the spent FeZn-Na catalyst was also responsible for the largest amount of H_2

desorption [50]. Moreover, compared with the other three catalysts, the desorption peaks of the FeCu-Na catalyst shifted toward a lower temperature, revealing that Cu was more favorable for the activation of H_2 [45].

According to the XPS data shown in Fig. 9, the binding energy of Fe $2p_{3/2}$ located at ca. 711.6 eV was attributed to Fe^{3+} species, indicating that Fe^{3+} was present on the surface of the pristine catalysts. It is worth noting that the Fe $2p_{3/2}$ peaks of FeCu-Na were shifted to lower binding energies in comparison to those of the other catalysts, further confirming that Cu acted as an electron promoter for transferring electrons to Fe. After the reaction of the Fe-Na, FeZn-Na, and FeMn-Na catalysts, their spectra exhibited a wide peak in the binding energy range of 710.6 – 710.8 eV , which could be ascribed to an overlap of the Fe^{2+} and Fe^{3+} signals, further confirming the presence of the Fe_3O_4 phase. Although XRD characterization clearly suggested the existence of the Fe_5C_2 phase for all the spent samples, only the FeZn-Na and FeCu-Na catalysts presented an obvious characteristic peak for Fe_5C_2 near the binding energy of 706.7 eV . The signal associated with Fe_5C_2 species was very weak on the surface of the spent Fe-Na catalyst and was not observed for FeMn-Na. Therefore, it was deduced that Zn and Cu promoted the carburization of the catalyst, while the Mn promoter hindered the formation of the surface Fe_5C_2 species. Moreover, the surface compositions of the pristine and spent catalysts derived from the XPS are given in Table S4. The surface ratio of Fe:Na for all the catalysts decreased significantly after the CO_2 hydrogenation reaction, indicating that the Na migrated to the surface of the spent catalysts.

3.5. Effect of transition metals on CO_2 conversion and CO formation

The catalytic stability of Fe-based catalysts plays a crucial role in their further applications, and their deactivation can be mainly attributed to the oxidation of Fe_5C_2 to Fe_3O_4 , as well as the growth and sintering of iron carbide [51,52]. CO_2 conversion and CO selectivity based on the analysis of gaseous products during 120 h of time-on-stream (TOS) are shown in Fig. 10. For the Fe-Na catalyst (Fig. 10a), CO_2 conversion declined continuously to 23.4 % after reaching a maximum of 36.0 %, while the selectivity toward CO increased continuously from 5.9 % after 4 h to 30.6 % after 120 h, indicating that the stability of the Fe-Na catalyst was relatively poor. Sintering of the iron species nanoparticles during the reaction might account for the severe deactivation of the Fe-Na catalyst, as suggested by the TEM of the spent Fe-Na.

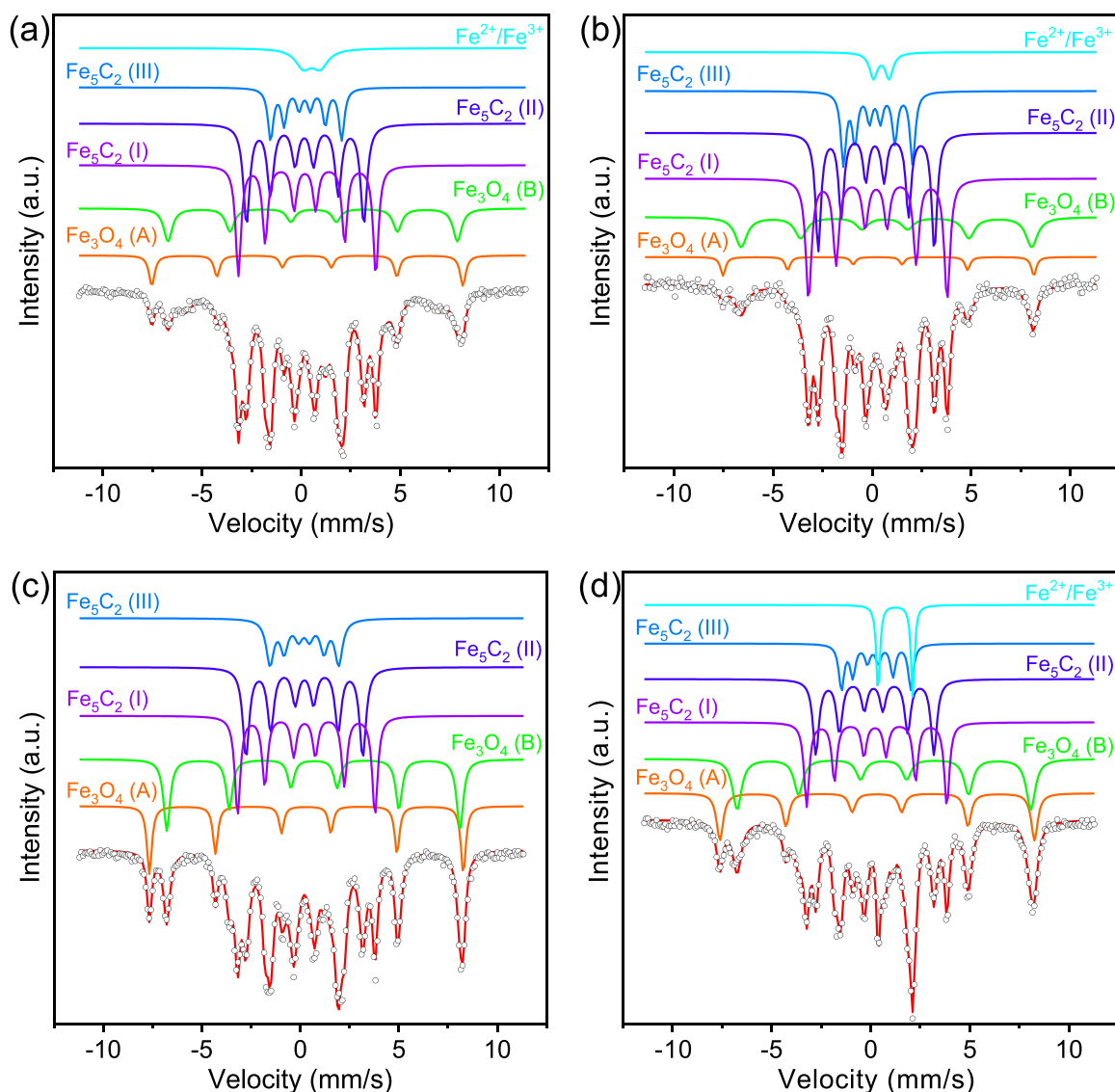


Fig. 7. Mössbauer spectra of the spent catalysts. (a) Fe-Na, (b) FeZn-Na, (c) FeCu-Na, and (d) FeMn-Na.

Therefore, it is highly desirable to improve the stability of Fe-based catalysts.

The introduction of all of the Zn, Cu, and Mn promoters improved the stability of the Fe-based catalysts. Among them, FeZn-Na presented the greatest long-time stability, whose catalytic performance remained unchanged after a 16 h induction period (Fig. 10b). In terms of the FeCu-Na (Fig. 10c) and FeMn-Na (Fig. 10d) catalysts, three apparent stages, including an induction period, deactivation period, and steady state could be observed with a TOS of 120 h. CO₂ conversion first increased, then decreased possibly due to the rapid agglomeration of iron species within the initial 40 h, and finally remained almost constant after reaction for 40 h TOS. CO selectivity increased gradually and afterward remained unchanged. Owing to the formation of ZnFe₂O₄ spinel, which led to strong interaction between Fe and Zn, agglomeration of the iron carbides and iron oxides obtained after initial structural evolution was hindered (Table S5), and the crystal size of Fe₃O₄ and Fe₅C₂ increased slightly from 40.5 nm and 39.4 nm at a TOS of 16 h to 44.6 nm and 42.2 nm at a TOS of 120 h. In addition, both the significantly enhanced activation of H₂, which suppressed the oxidation of Fe₅C₂, and the stabilization effect of Zn on Fe₅C₂ contribute to the remarkable stability of the FeZn-Na catalyst.

As presented in Fig. 10, during the induction period, CO₂ conversion

increased rapidly until a maximum was reached. For the Fe-Na, FeZn-Na, and FeMn-Na catalysts, the highest CO₂ conversion of 36–38 % was achieved at 16 h. Although the equilibrium conversion of CO₂ in the RWGS reaction is 25.8 % at 320 °C with a H₂/CO₂ ratio of 3, the formations of olefins and paraffins from CO₂ and H₂ are highly favored at this temperature due to their exothermicities (Fig. S8). Therefore, it is possible to significantly increase the equilibrium conversion of CO₂ at 320 °C. The FeCu-Na catalyst achieved its peak performance after 12 h, with a CO₂ conversion of 34.7 %. The H₂-TPR profiles showed that the incorporation of Cu significantly enhanced the reduction of Fe species due to its intrinsic activity toward H₂. In addition, Cu was active in the RWGS reaction, and the enhanced concentration of CO accelerated the reduction and carburization of Fe species, possibly explaining why the FeCu-Na catalyst peaked earlier than the other catalysts. Moreover, the intrinsic activity was determined to evaluate the catalytic behavior of the catalysts. All of the transition metal-modified catalysts exhibited enhanced catalytic activity for CO₂ conversion due to the enhanced CO₂ adsorption strength of the catalysts (Table 1). Among them, the FeZn-Na catalyst delivered the highest intrinsic activity of 33.2 mmol CO₂ g_{Fe}⁻¹ h⁻¹, much higher than that of the Fe-Na (23.9 mmol CO₂ g_{Fe}⁻¹ h⁻¹) catalyst.

After this, from 12 or 16–40 h, the FeCu-Na and FeMn-Na catalysts

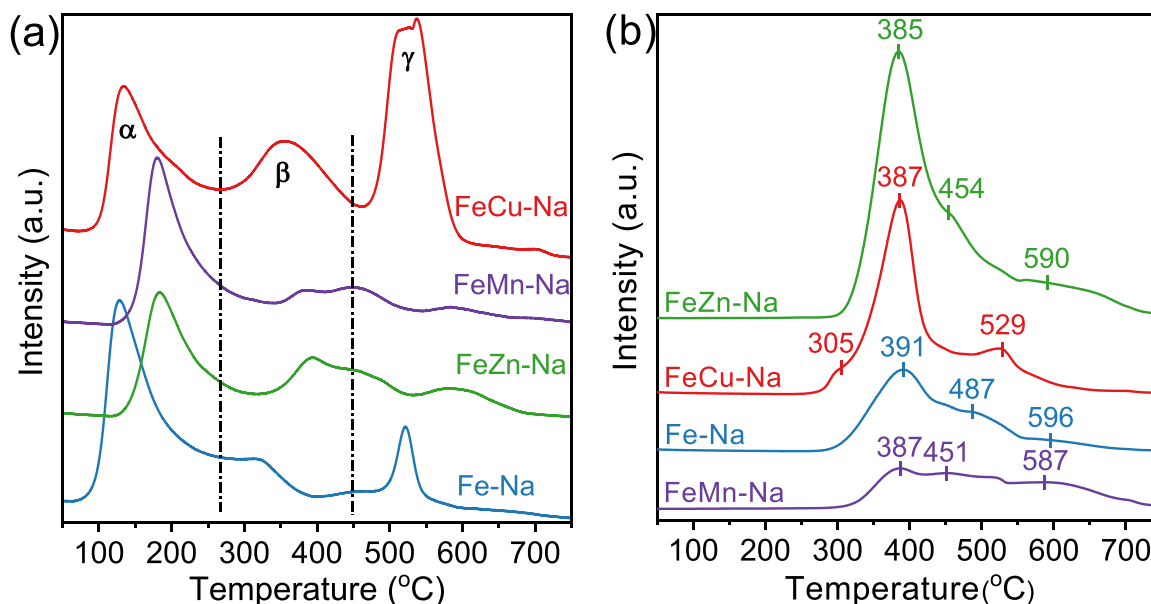


Fig. 8. (a) CO₂-TPD and (b) H₂-TPD profiles of the Fe-based catalysts.

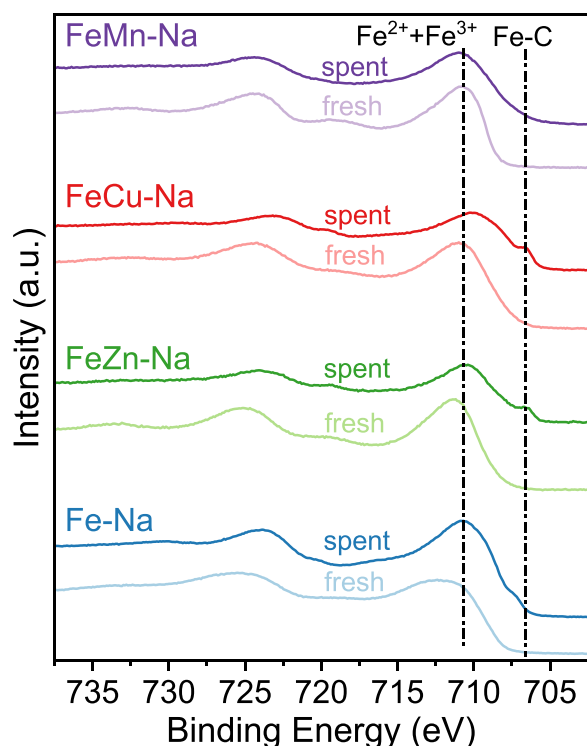


Fig. 9. XPS spectra of the Fe-based catalysts.

showed gradual deactivation to varying extents. CO₂ conversion over the FeCu-Na and FeMn-Na catalysts decreased from 34.7 % to 29.9 % and 36.7–30.2 %, respectively. Meanwhile, the selectivity toward CO of the transition metal-modified catalysts increased gradually over the initial 40 h and afterwards remained almost unchanged. The selectivity toward CO at a TOS of 40 h over the FeCu-Na catalyst was slightly higher than for Fe-Na, which was attributed to the promotion of the RWGS reaction by metallic Cu. The FeMn-Na catalyst exhibited significantly higher selectivity toward CO at a TOS of 40 h than the other catalysts. The much lower content of iron carbide and the weakened interaction between the iron species and CO hindered the subsequent conversion of

CO intermediates on the FeMn-Na catalyst, resulting in a higher amount of unconverted CO. In the stable stage, the highest CO₂ conversion of 37.5 % and the lowest CO selectivity of 11.5 % were obtained over the FeZn-Na catalyst. The smaller particle size derived from the spinel structure was beneficial for the activation of H₂ and transformation of CO₂. Additionally, the enrichment of both Na and Zn species on the external surface of Fe promoted the chemisorption of CO and the subsequent carburization of iron species, which favored a shift in the reaction equilibrium and drove the conversion of CO₂.

3.6. The effect of transition metals on hydrocarbon distributions

The selectivities of gas and liquid products in the stable stage were normalized, and the catalytic performances are summarized in Table 1 and Fig. 11. From the data, it can be seen that even the Fe-Na catalyst displayed high selectivity toward olefins, where the total olefin selectivity was 66.5 %, with the selectivities of C₂₋₄ and C₅₊ olefins being 41.4 % and 25.1 %, respectively. The olefin-to-paraffin (O/P) ratios in the ranges of C₂₋₄ and C₅₊ were 5.2 and 3.4, respectively. Among the transition metal-decorated catalysts, the FeZn-Na catalyst delivered the highest olefin selectivity of 69.2 %, in which the proportions of C₂₋₄ and C₅₊ were 36.9 % and 32.3 %, respectively. The FeZn-Na catalyst also showed the highest olefin STY of 138 mg g_{cat}⁻¹ h⁻¹. Additionally, the maximum O/P ratios of the C₂₋₄ and C₅₊ hydrocarbons were 5.5 and 3.6, respectively, and an α value of 0.61 was obtained over the FeZn-Na catalyst. These results indicated that Zn modification not only significantly promoted the conversion of CO₂ but also facilitated the generation of olefins and the carbon chain propagation. However, the phase separation between the Fe and Cu species resulted in the lower chain propagation activity of FeCu-Na compared with FeZn-Na and FeMn-Na, with a lower α value of 0.56. In addition, the olefin selectivity over the FeCu-Na catalyst was relatively low (62.2 %), and the O/P ratios of the C₂₋₄ and C₅₊ hydrocarbons were the lowest at only 3.3 and 3.0, respectively, among all of the catalysts. According to H₂-TPD analysis, the working FeZn-Na catalyst also possessed a large amount of adsorbed H atoms, even higher than for the FeCu-Na catalyst. However, the FeZn-Na catalyst exhibited a much higher O/P ratio than that of the FeCu-Na catalyst, indicating that the O/P ratio was dependent on other factors, as discussed in the following. The FeMn-Na catalyst exhibited the highest selectivity toward C₂₋₄ of 41.9 % and the lowest toward C₅₊ of 21.6 %. The weakened interaction between Fe and CO may have resulted in a

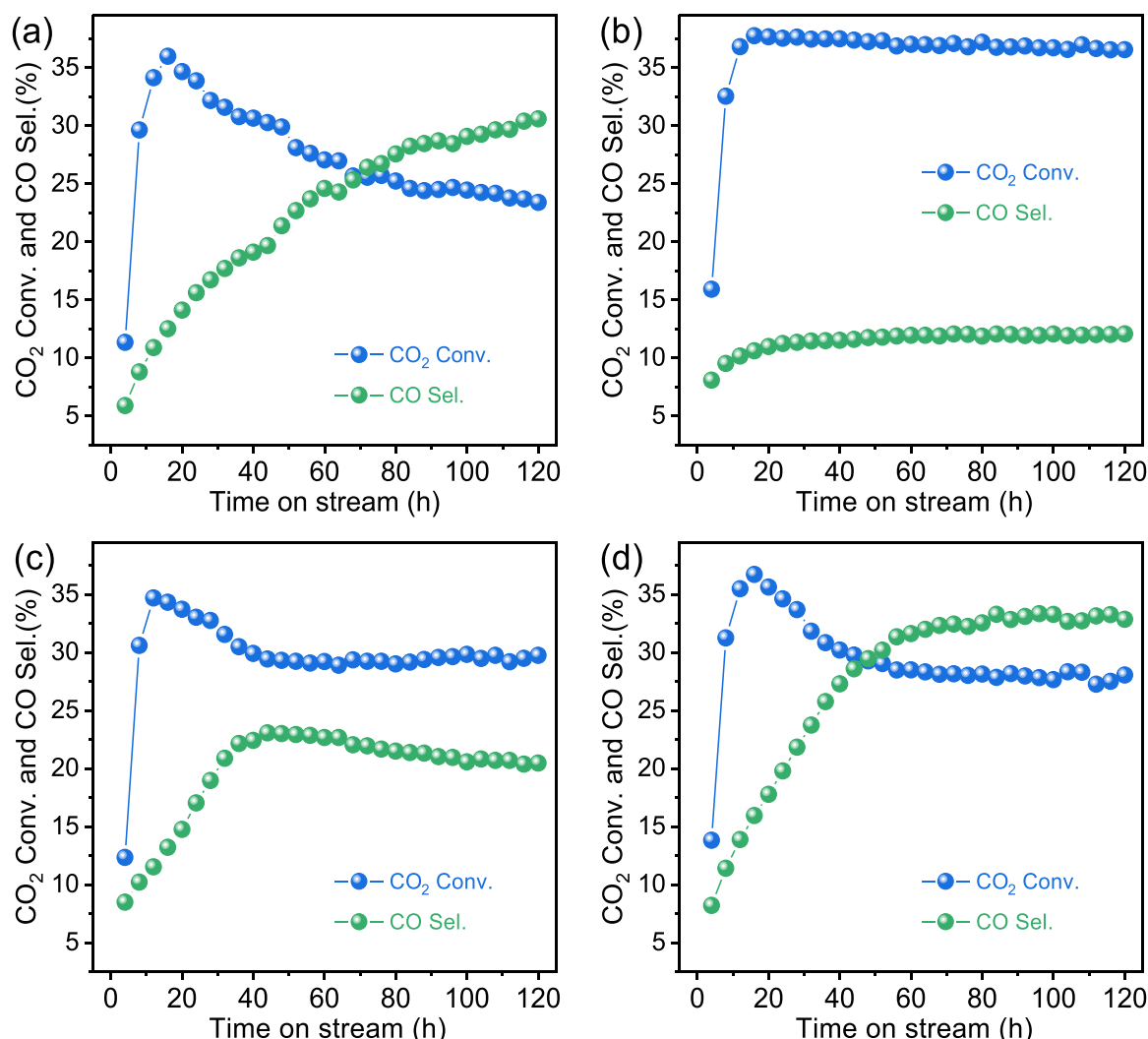


Fig. 10. Stability test of the Fe-based catalysts. (a) Fe-Na, (b) FeZn-Na, (c) FeCu-Na, and (d) FeMn-Na. Standard reaction conditions: 320 °C, 3 MPa, 4000 mL g_{cat}⁻¹ h⁻¹, and H₂/CO₂/N₂ = 73/24/3.

Table 1

Catalytic performance of the Fe-based catalysts.

Sample	CO ₂ Conv. (%)	CO Sel. (%)	Hydrocarbon distribution (%)					O/P ^a		Activity ^b (mmol CO ₂ g _{Fe} ⁻¹ h ⁻¹)	STY of olefins (mg g _{cat} ⁻¹ h ⁻¹)
			CH ₄	C ₂₋₄ ^o	C ₂₋₄ ⁼	C ₅₊ ^o	C ₅₊ ⁼	C ₂₋₄	C ₅₊		
Fe-Na	30.6	19.1	18.2	7.9	41.4	7.3	25.1	5.2	3.4	23.9	99.8
FeZn-Na	37.5	11.5	15.0	6.8	36.9	9.0	32.3	5.5	3.6	33.2	138.0
FeCu-Na	29.9	22.4	18.3	11.6	38.1	7.9	24.1	3.3	3.0	29.6	86.6
FeMn-Na	30.2	26.3	19.2	10.4	41.9	6.9	21.6	4.0	3.1	30.2	84.8

Standard reaction conditions: 320 °C, 3 MPa, 4000 mL g_{cat}⁻¹ h⁻¹, H₂/CO₂/N₂ = 73/24/3, and TOS = 40 h. ^a The ratio of olefin to paraffin. ^b The activity represents the CO₂ conversion rate normalized by the weight of Fe at the maximum of CO₂ conversion.

lower proportion of C species being present on the surface of the FeMn-Na catalyst, which inhibited chain growth and favored the formation of lighter olefins. In addition,

CO₂ hydrogenation is an exothermal reaction, and heat transfer in the catalyst bed may influence the catalytic performance. Therefore, we investigated effect of space velocity on the catalytic performance over the FeZn-Na catalyst. As shown in Fig. S9, the hydrocarbon distribution of the catalyst remains almost unchanged at the increasing space velocity.

The secondary hydrogenation capability of the formed olefins on the active sites of the working catalysts played a pivotal role in affecting the

O/P ratio [46,48,53,54]. Inspired by this, C₃H₆-PTH experiments were conducted to explore whether the olefins preferably desorb from or hydrogenate on the activated catalysts in the presence or absence of the transition-metal promoters. Prior to the C₃H₆-PTH measurements, the catalysts were in situ reduced and reacted for 40 h under the reaction conditions. C₃H₆ and C₃H₈ signals were recorded synchronously, and the results showed that all of the catalysts had the ability to convert olefins into paraffins under a flow of H₂ (Fig. 12). The R value, representing the ratio of the integral area of C₃H₆ to that of C₃H₈, is indicative of the ability of olefins to be hydrogenated. The R value decreased in the order of FeZn-Na (10.8) > Fe-Na (9.0) > FeMn-Na (7.2) > FeCu-Na (4.8). The

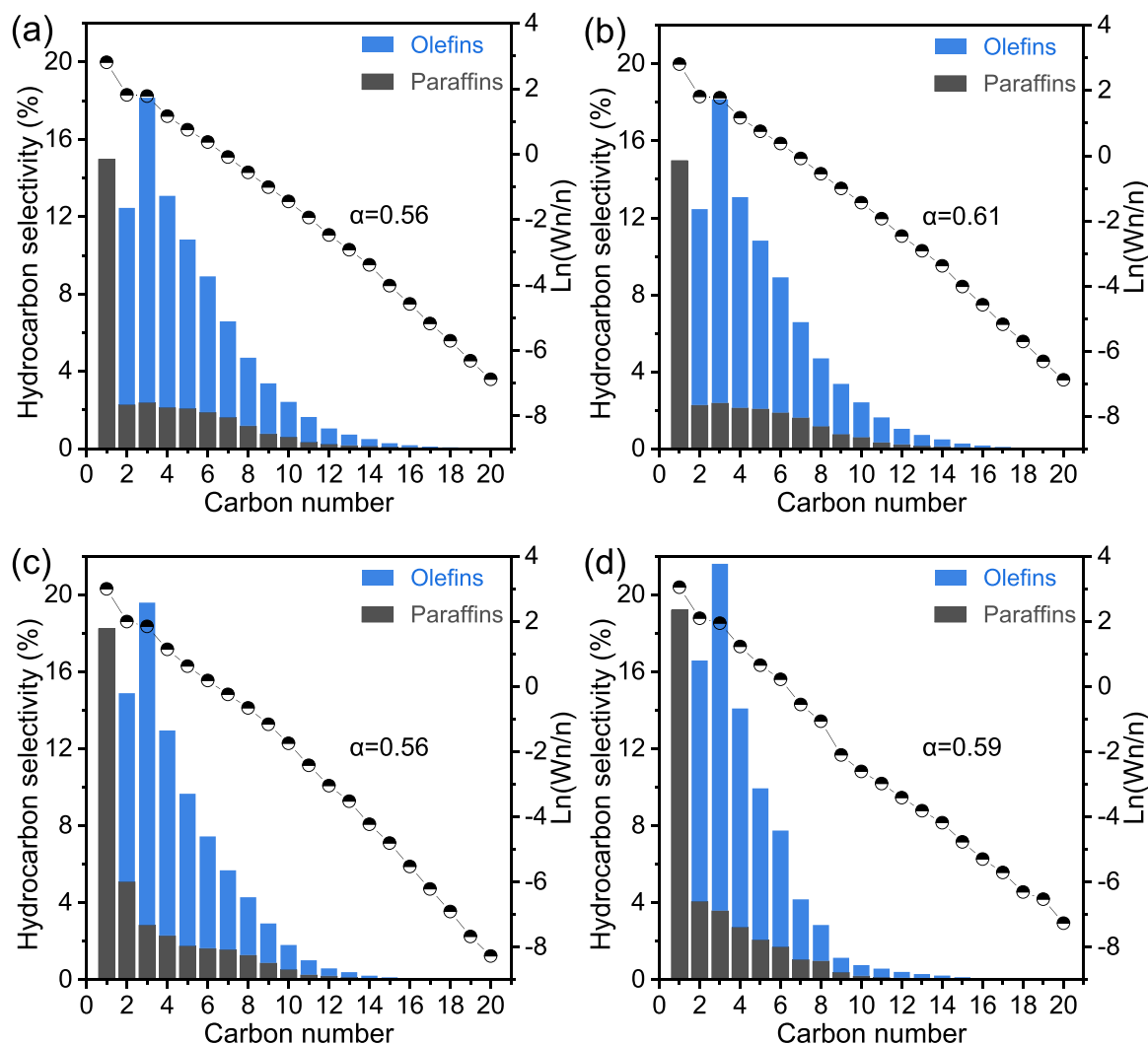


Fig. 11. Distribution of the hydrocarbons. (a) Fe-Na, (b) FeZn-Na, (c) FeCu-Na, and (d) FeMn-Na.

O/P ratio in the C_{2-4} range was found to increase linearly with the increasing R value (Fig. S10). These results suggested that the lower the R value, the more likely the catalyst to hydrogenate the formed olefins. It has been reported that the presence of Na can inhibit the secondary hydrogenation of olefins by weakening olefin adsorption on the surface of iron catalysts. In this work, all of the catalysts had a similar bulk Na content of approximately 2.5 wt%, as well as a similar surface Fe:Na ratio of 0.8 after reaction for 40 h, as evidenced by XPS analysis. However, the catalysts exhibited very different secondary hydrogenation ability toward the formed olefins on their working surfaces. More specifically, the addition of Zn remarkably inhibited the further hydrogenation of olefins on the working surface of the FeZn-Na catalyst, whereas the Cu promoter enhanced the capability of secondary olefin hydrogenation and yielded a much lower O/P ratio than for the other catalysts.

3.7. DFT calculations

To a first approximation, the O/P ratio is controlled by the hydrogenation ability of the working iron catalyst surface, which can hydrogenate the formed olefin intermediates adsorbed on the catalyst surface. To verify the above theoretical hypothesis and rationalize the trend in the experimental observations in this work, first-principles calculations were conducted for the reaction pathways of the hydrogenation of propene to propane at the interfacial sites of the Cu/Fe₅C₂ and ZnO/

Fe₅C₂, which were compared to that over the Fe₅C₂ alone. Based on the above experimental characterization, the Fe₅C₂(111) surface was chosen to model the Fe₅C₂ component of the catalysts, whereas two extended rows of Cu atoms over the Fe₅C₂(111) surface were used to model the metallic Cu component in the Cu/Fe₅C₂, with a similar model adopted for the ZnO component in the ZnO/Fe₅C₂. The optimized Cartesian coordinates for these catalyst models are given in Table S6–S8.

Fig. 13 shows a comparison of the potential energy surface for C₃H₆ hydrogenation to C₃H₈ over the Fe₅C₂(111) and Cu/Fe₅C₂(111) surfaces, which consisted of two elementary hydrogenation steps. For the first hydrogenation step (C₃H₆* + H* → C₃H₇* + *, * denotes the active sites), the calculated energy barrier at the Cu/Fe₅C₂(111) interface is negligible at 0.06 eV, much lower than that over the Fe₅C₂(111) surface of 0.65 eV, as listed in Table S9. For the second hydrogenation step (C₃H₇* + H* → C₃H₈* + *), the calculated energy barriers over both surfaces were much higher at 0.80 eV and 0.95 eV for the Cu/Fe₅C₂(111) and Fe₅C₂(111) surfaces (Table S9), respectively, indicating that this step is the rate-determining step (RDS) for this reaction. More importantly, the energy barrier of this RDS was predicted to be substantially lowered by forming the Cu/Fe₅C₂(111) interface, suggesting that the Cu/Fe₅C₂(111) interface favors the further hydrogenation of the formed olefins to saturated hydrocarbons. This was consistent with both the lower R value observed in the C₃H₆-PTH experiments over the FeCu-Na catalyst (4.8 vs. 9.0 for Fe-Na) and the lower O/P value over this catalyst during CO₂ hydrogenation (3.3 vs. 5.2 for Fe-Na). The

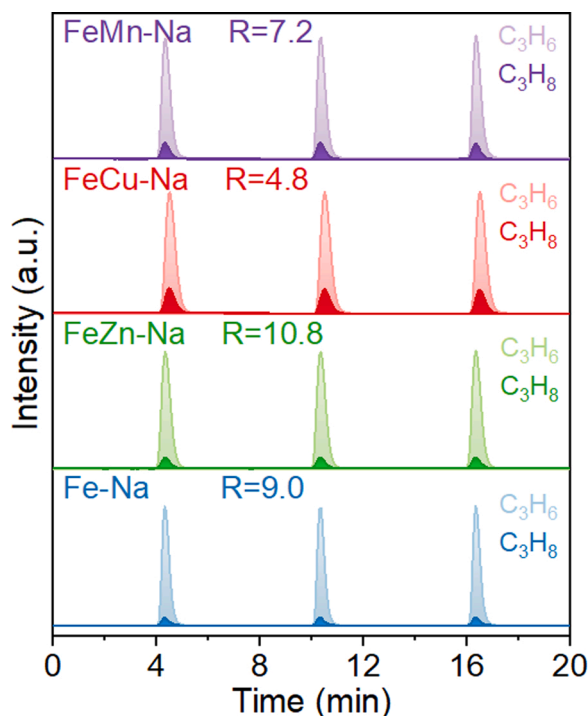


Fig. 12. C_3H_6 pulse reactions of the spent catalysts.

consistency between the theoretical and experimental results supported the above theoretical hypothesis.

Fig. 14a and b show a further comparison of the adsorption structures of C_3H_6 over the $Cu/Fe_5C_2(111)$ and $ZnO/Fe_5C_2(111)$ interfaces. Compared with the $Cu/Fe_5C_2(111)$ interfacial structure, where the two rows of Cu atoms were fairly well-aligned, the $ZnO/Fe_5C_2(111)$ interfacial structure was significantly more complex, where two zigzag $Zn-O-Zn-O$ chains were formed and the Zn(O) atoms were surrounded by two or three O(Zn) atoms besides their interaction with the underlying $Fe_5C_2(111)$ surface. Due to the greater complexity of the $ZnO/Fe_5C_2(111)$ interface, only the adsorption energy of C_3H_6 was determined over this surface, which was compared with that at the $Cu/Fe_5C_2(111)$ interface. As also shown in Table S10, the adsorption of C_3H_6 was predicted to be only slightly stronger at the $Cu/Fe_5C_2(111)$ interface (-0.53 eV), compared with at the $Fe_5C_2(111)$ surface (-0.46 eV), where the more negative adsorption energy suggested more favorable C_3H_6 adsorption on the catalyst surface. As further shown in Fig. S11, direct

comparison of the adsorption structures on these two surfaces suggest that on the $Fe_5C_2(111)$ surface the two C atoms in the C_3H_6 both bind the same surface Fe atom at the same C-Fe distances of 2.17 Å, whereas at the $Cu/Fe_5C_2(111)$ interface the terminal C atom in C_3H_6 further binds the interfacial Cu site (C-Cu: 2.53 Å) besides the two C-Fe bonds of 2.12 and 2.18 Å. This is consistent with the stronger adsorption on the $Cu/Fe_5C_2(111)$ interface and its longer C-C “double” bond of 1.43 Å compared to that of 1.40 Å on the $Fe_5C_2(111)$ surface. In sharp contrast, a similar adsorption structure of C_3H_6 at the $ZnO/Fe_5C_2(111)$ interface was found to be highly unstable, with a very positive adsorption energy of 1.65 eV, suggesting that the chemical interaction of C_3H_6 with this interface was unfavorable. As further shown in Fig. S12, the terminal C in C_3H_6 was predicted to interact with the surface O leading to a destabilized radical structure. We note that physisorption of C_3H_6 at this interface was still possible, although such interaction was much weaker, as indicated by the very weak predicted physisorption of the product C_3H_8 over all three surfaces. The unfavorable chemical interaction of C_3H_6 with the $ZnO/Fe_5C_2(111)$ interface facilitated its desorption from the catalyst surface and prevented it from further hydrogenating, which was consistent with it exhibiting the highest R value in the C_3H_6 -PTH measurements (10.8) and the highest O/P value during CO_2 hydrogenation (5.5). The fact that saturated hydrocarbons still formed over the $FeZn-Na$ catalyst might be attributed to the $Fe_5C_2(111)$ surfaces distant from the $ZnO/Fe_5C_2(111)$ interface, i.e. the interfacial effects were possibly short ranged.

To further rationalize the great difference between the calculated C_3H_6 adsorption energies over the different model surfaces, charge density differences ($\Delta\rho$) before and after its adsorption were plotted. As shown in Fig. 14c for the $Cu/Fe_5C_2(111)$ interface, this interface is electron rich due to substantial electron transfer from the Cu atoms to the $Fe_5C_2(111)$ surface, which was estimated to be $1.17e$ from Bader atomic charge analysis, which facilitated the adsorption of C_3H_6 . Close inspection of Fig. 14a and c suggests that the C_3H_6 adsorbate interacted via its π/π^* states in the $C=C$ double bond with a surface Fe site in the electron accumulation region. In contrast, for the $ZnO/Fe_5C_2(111)$ interface, electron transfer from the ZnO cluster to the $Fe_5C_2(111)$ surface was much less pronounced, with only $0.53e$, while the Zn ions were electron-deficient and the O ions were electron rich, which might have been detrimental to the chemical adsorption of C_3H_6 at the surface Fe sites. Fig. 14b and d show that C_3H_6 was no longer adsorbed at the Fe site on the $Fe_5C_2(111)$ surface but at the electron-rich region of the ZnO cluster, which was energetically highly unfavorable.

Our DFT calculations thus showed that the further adsorption and hydrogenation of olefins was unfavorable at the ZnO/Fe_5C_2 interface, whereas it was promoted at the Cu/Fe_5C_2 interface, which was

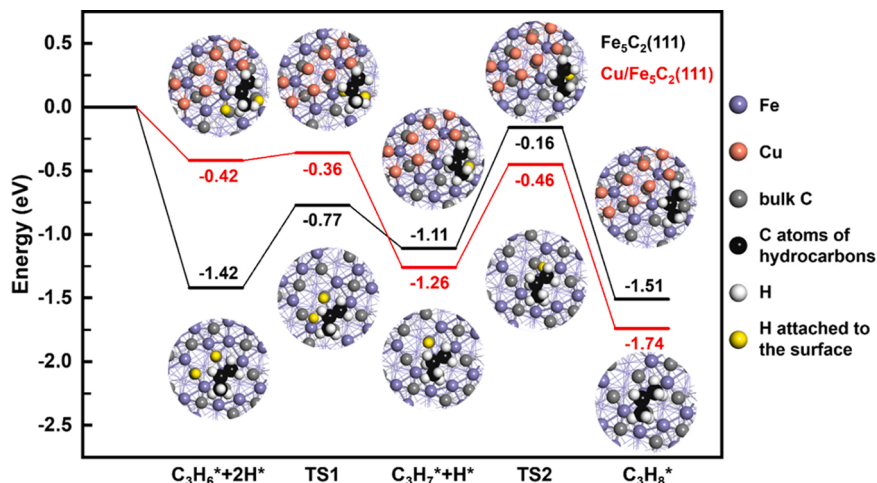


Fig. 13. Reaction pathways for propene hydrogenation into propane on the $Fe_5C_2(111)$ (black line) and $Cu/Fe_5C_2(111)$ (red line) surfaces.

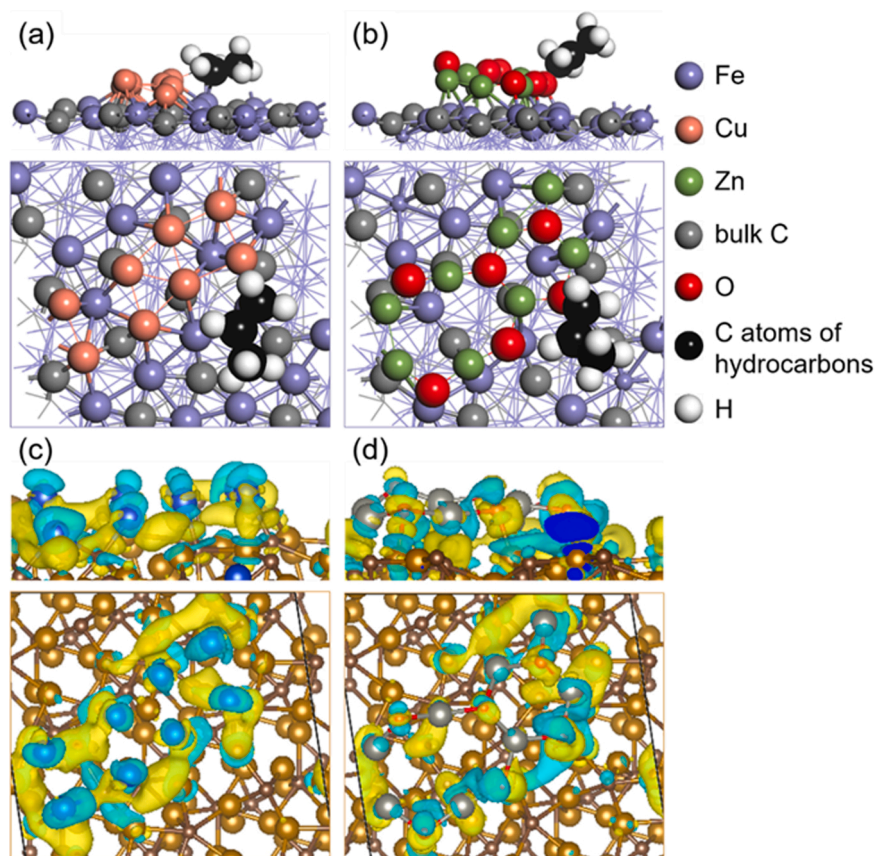


Fig. 14. Adsorption structures of propene on the (a) Cu/Fe₅C₂(111) and (b) ZnO/Fe₅C₂(111) surfaces; charge density difference plots upon adsorption at the (c) copper strip and (d) ZnO strip on the Fe₅C₂(111) surface, respectively, where the light blue region represents charge depletion and the light yellow region represents charge accumulation.

consistent with the results of the C₃H₆-PTH and CO₂ hydrogenation experiments.

4. Conclusions

In summary, the promoting effects that Zn, Cu, and Mn have on the physicochemical properties and catalytic performance of Fe-based catalysts during the hydrogenation of CO₂ were investigated. Zn and Cu modifiers were found to promote the reduction and carburization of the iron catalysts, and benefit the formation of Fe₃O₄ and Fe₅C₂ active phases, while also remarkably enhancing the surface basicity and activation of H₂. Although the introduction of Mn enhanced the reducibility of iron oxides, the strong interaction between Mn and the iron species inhibited the chemical adsorption of CO and the carburization of the FeMn-Na catalyst, thus disfavoring the further conversion of CO intermediates. Therefore, the highest CO₂ hydrogenation activity and lowest CO selectivity were achieved over the FeZn-Na catalyst. By further combining the results of C₃H₆-PTH experiments and DFT calculations, zinc oxide was found to inhibit the secondary hydrogenation of olefins on the working catalyst by promoting the desorption of C₃H₆ from the catalyst at the ZnO/Fe₅C₂(111) interface. This accounts for the observation that the FeZn-Na catalyst exhibited excellent performance in terms of olefin selectivity (69.2 %) and the highest O/P ratios of 5.5 and 3.6 in the C₂₋₄ and C₅₊ ranges, respectively. However, the Cu species was found to enhance the secondary hydrogenation of the so-formed olefins, thus yielding a much lower O/P ratio than for the other studied catalysts, which is mostly due to the lower energy barrier of the RDS for the secondary hydrogenation reaction at the Cu/Fe₅C₂(111) interface compared with the pristine Fe₅C₂(111) surface. This experimental and computational study not only provides a better understanding of the

effect that each transition-metal promoter has on the catalytic performance, but also suggests that tuning the olefin adsorption energy and hydrogenation barrier is a viable approach in optimizing the O/P ratio in CO₂/CO-to-olefin reactions.

CRediT authorship contribution statement

Haiyan Yang: Conceptualization, Methodology, Investigation, Formal analysis, Writing – original draft. **Yaru Dang:** Formal analysis, Investigation, Writing – original draft. **Xu Cui:** Methodology, Investigation. **Xianni Bu:** Investigation. **Jiong Li:** Investigation. **Shenggang Li:** Supervision, Methodology, Writing – review & editing. **Yuhan Sun:** Supervision, Conceptualization. **Peng Gao:** Supervision, Conceptualization, Methodology, Funding acquisition, Writing – review & editing.

Declaration of Competing Interest

The authors declare that they have no known competing financial interests or personal relationships that could have appeared to influence the work reported in this paper.

Data availability

Data will be made available on request.

Acknowledgements

X-Ray absorption measurements were performed at the BL11B beamline at the Shanghai Synchrotron Radiation Facility (SSRF), Shanghai, P. R. China. This work was financially supported by the

National Natural Science Foundation of China (22172189, 21773286, 22172188), Youth Innovation Promotion Association CAS (2018330), Program of Shanghai Academic Research Leader (22XD1424100), Doctoral Research Startup Foundation of Hebei Normal University of Science and Technology (304050224), and Joint Fund of the Yulin University and the Dalian National Laboratory for Clean Energy (Grant. YLU-DNL Fund 2022001).

Appendix A. Supporting information

Supplementary data associated with this article can be found in the online version at [doi:10.1016/j.apcatb.2022.122050](https://doi.org/10.1016/j.apcatb.2022.122050).

References

- [1] J. Wei, R.W. Yao, Y. Han, Q.J. Ge, J. Sun, Towards the development of the emerging process of CO₂ heterogeneous hydrogenation into high-value unsaturated heavy hydrocarbons, *Chem. Soc. Rev.* 50 (2021) 10764–10805.
- [2] W. Zhou, K. Cheng, J.C. Kang, C. Zhou, V. Subramanian, Q.H. Zhang, Y. Wang, New horizon in C1 chemistry: breaking the selectivity limitation in transformation of syngas and hydrogenation of CO₂ into hydrocarbon chemicals and fuels, *Chem. Soc. Rev.* 48 (2019) 3193–3228.
- [3] P. Gao, L.N. Zhang, S.G. Li, Z.X. Zhou, Y.H. Sun, Novel heterogeneous catalysts for CO₂ hydrogenation to liquid fuels, *ACS Catal. Sci.* 6 (2020) 1657–1670.
- [4] P. Gao, S.G. Li, X.N. Bu, S.S. Dang, Z.Y. Liu, H. Wang, L.S. Zhong, M.H. Qiu, C. G. Yang, J. Cai, W. Wei, Y.H. Sun, Direct conversion of CO₂ into liquid fuels with high selectivity over a bifunctional catalyst, *Nat. Chem.* 9 (2017) 1019–1024.
- [5] M.K. Khan, P. Butolia, H. Jo, M. Irshad, D. Han, K.W. Nam, J. Kim, Selective conversion of carbon dioxide into liquid hydrocarbons and long-chain α -olefins over Fe-amorphous AlOx bifunctional catalysts, *ACS Catal.* 10 (2020) 10325–10338.
- [6] Z.X. Zhou, P. Gao, CO₂ hydrogenation to high-value products via heterogeneous catalysis, *Chin. J. Catal.* 43 (2022) 2045–2056.
- [7] J.H. Liu, Y.K. Song, X.M. Guo, C.S. Song, X.W. Guo, Recent advances in application of iron-based catalysts for COx hydrogenation to value-added hydrocarbons, *Chin. J. Catal.* 43 (2022) 731–754.
- [8] J. Skupinska, Oligomerization of α -olefins to higher oligomers, *Chem. Rev.* 91 (1991) 613–648.
- [9] T. Numpilai, C.K. Cheng, J. Limtrakul, T. Witoon, Recent advances in light olefins production from catalytic hydrogenation of carbon dioxide, *Process Saf. Environ.* 151 (2021) 401–427.
- [10] Y.L. Zhang, C.X. Cao, C. Zhang, Z.P. Zhang, X.L. Liu, Z.X. Yang, M.H. Zhu, B. Meng, J. Xu, Y.F. Han, The study of structure-performance relationship of iron catalyst during a full life cycle for CO₂ hydrogenation, *J. Catal.* 378 (2019) 51–62.
- [11] Z.Q. Zhang, H.R. Yin, G.D. Yu, S. He, J.C. Kang, Z.M. Liu, K. Cheng, Q.H. Zhang, Y. Wang, Selective hydrogenation of CO₂ and CO into olefins over sodium- and zinc-promoted iron carbide catalysts, *J. Catal.* 395 (2021) 350–361.
- [12] S. Yang, H.J. Chun, S. Lee, S.J. Han, K.Y. Lee, Y.T. Kim, Comparative study of olefin production from CO and CO₂ using Na- and K-promoted zinc ferrite, *ACS Catal.* 10 (2020) 10742–10759.
- [13] S.W. Wang, T.J. Wu, J. Lin, Y.S. Ji, S.R. Yan, Y. Pei, S.H. Xie, B.N. Zong, M.H. Qiao, Iron-potassium on single-walled carbon nanotubes as efficient catalyst for CO₂ hydrogenation to heavy olefins, *ACS Catal.* 10 (2020) 6389–6401.
- [14] Y. Xu, P. Zhai, Y.C. Deng, J.L. Xie, X. Liu, S. Wang, D. Ma, Highly selective olefin production from CO₂ hydrogenation on iron catalysts: a subtle synergy between manganese and sodium additives, *Angew. Chem. Int. Ed.* 59 (2020) 21736–21744.
- [15] H.M. Torres Galvis, A.C.J. Koeken, J.H. Bitter, T. Davidian, M. Ruitenbeek, A. I. Dugulan, K.P. de Jong, Effects of sodium and sulfur on catalytic performance of supported iron catalysts for the Fischer-Tropsch synthesis of lower olefins, *J. Catal.* 303 (2013) 22–30.
- [16] B.L. Liang, H.M. Duan, T. Sun, J.G. Ma, X. Liu, J.H. Xu, X. Su, Y.Q. Huang, T. Zhang, Effect of Na promoter on Fe-based catalyst for CO₂ hydrogenation to alkenes, *ACS Sustain. Chem. Eng.* 7 (2019) 925–932.
- [17] J. Wei, J. Sun, Z.Y. Wen, C.Y. Fang, Q.J. Ge, H.G. Xu, New insights into the effect of sodium on Fe₃O₄-based nanocatalysts for CO₂ hydrogenation to light olefins, *Catal. Sci. Technol.* 6 (2016) 4786–4793.
- [18] X. Wang, J.L. Zhang, J.Y. Chen, Q.X. Ma, S.B. Fan, T.S. Zhao, Effect of preparation methods on the structure and catalytic performance of Fe-Zn/K catalysts for CO₂ hydrogenation to light olefins, *Chin. J. Chem. Eng.* 26 (2018) 761–767.
- [19] R. Adrian, G. Lieven, B. Anastasiya, O.C. Samy, G. Jorge, Metal organic framework-derived iron catalysts for the direct hydrogenation of CO₂ to short chain olefins, *ACS Catal.* 8 (2018) 9174–9182.
- [20] B.L. Liang, J.G. Ma, H.M. Duan, L. Li, X.L. Yang, Y.R. Zhang, X. Su, Y.Q. Huang, T. Zhang, Mn decorated Na/Fe catalysts for CO₂ hydrogenation to light olefins, *Catal. Sci. Technol.* 9 (2018) 456–464.
- [21] Y. Han, C.Y. Fang, X.W. Ji, J. Wei, Q.J. Ge, J. Sun, Interfacing with carbonaceous potassium promoters boosts catalytic CO₂ hydrogenation of iron, *ACS Catal.* 10 (2020) 12098–12108.
- [22] C.G. Visconti, M. Martinelli, L. Falbo, A. Infantes-Molina, L. Lietti, P. Forzatti, G. Iaquaniello, E. Palo, B. Picutti, F. Brignoli, CO₂ hydrogenation to lower olefins on a high surface area K-promoted bulk Fe-catalyst, *Appl. Catal. B Environ.* 200 (2017) 530–542.
- [23] J.L. Zhang, S.P. Lu, X.J. Su, S.B. Fan, Q.X. Ma, T.S. Zhao, Selective formation of light olefins from CO₂ hydrogenation over Fe-Zn-K catalysts, *J. CO₂ Util.* 12 (2015) 95–100.
- [24] N. Chaiyapraditgul, T. Numpilai, C.K. Cheng, N. Siri-Nguan, T. Sornchamni, C. Wattanakit, J. Limtrakul, T. Witoon, Tuning interaction of surface-adsorbed species over Fe/K-Al₂O₃ modified with transition metals (Cu, Mn, V, Zn or Co) on light olefins production from CO₂ hydrogenation, *Fuel* 283 (2021), 119248.
- [25] Z.Z. Zhang, C.Y. Wei, L.Y. Jia, Y.Y. Liu, C. Sun, P. Wang, W.F. Tu, Insights into the regulation of FeNa catalysts modified by Mn promoter and their tuning effect on the hydrogenation of CO₂ to light olefins, *J. Catal.* 390 (2020) 12–22.
- [26] W.B. Gong, R.P. Ye, J. Ding, T.T. Wang, X.F. Shi, C.K. Russell, J.K. Tang, E. G. Eddings, Y.L. Zhang, M.H. Fan, Effect of copper on highly effective Fe-Mn based catalysts during production of light olefins via Fischer-Tropsch process with low CO₂ emission, *Appl. Catal. B Environ.* 278 (2020), 119302.
- [27] K.Y. Kim, H. Lee, W.Y. Noh, J. Shin, S.J. Han, S.K. Kim, K. An, J.S. Lee, Cobalt ferrite nanoparticles to form a catalytic Co-Fe alloy carbide phase for selective CO₂ hydrogenation to light olefins, *ACS Catal.* 10 (2020) 8660–8671.
- [28] L.S. Guo, J. Li, Y. Cui, R. Kosol, Y. Zeng, G.B. Liu, J.H. Wu, T.S. Zhao, G.H. Yang, L. S. Shao, P. Zhan, J.N. Chen, N. Tsubaki, Spinel-structure catalyst catalyzing CO₂ hydrogenation to full spectrum alkenes with an ultra-high yield, *Chem. Commun.* 56 (2020) 9372–9375.
- [29] W.J. Wang, X. Jiang, X.X. Wang, C.S. Song, Fe-Cu bimetallic catalysts for selective CO₂ hydrogenation to olefin-rich C₂₊ hydrocarbons, *Ind. Eng. Chem. Res.* 57 (2018) 4535–4542.
- [30] W.F. Tu, C. Sun, Z.Z. Zhang, W.Q. Liu, H.S. Malhi, W. Ma, M.H. Zhu, Y.F. Han, Chemical and structural properties of Na decorated Fe₃C₂-ZnO catalysts during hydrogenation of CO₂ to linear α -olefins, *Appl. Catal. B Environ.* 298 (2021), 120567.
- [31] A.J. Barrios, D.V. Peron, A. Chakkingal, A.I. Dugulan, S. Moldovan, K. Nakouri, J. Thuriot-Roukos, R. Wojcieszak, J.W. Thybaut, M. Virginie, A.Y. Khodakov, Efficient promoters and reaction paths in the CO₂ hydrogenation to light olefins over zirconia-supported iron catalysts, *ACS Catal.* 12 (2022) 3211–3225.
- [32] Y.H. Choi, Y.J. Jang, H. Park, W.Y. Kim, Y.H. Lee, S.H. Choi, J.S. Lee, Carbon dioxide Fischer-Tropsch synthesis: a new path to carbon-neutral fuels, *Appl. Catal. B Environ.* 202 (2017) 605–610.
- [33] J.H. Liu, A.F. Zhang, X. Jiang, M. Liu, Y.W. Sun, C.S. Song, X.W. Guo, Selective CO₂ hydrogenation to hydrocarbons on Cu-promoted Fe-based catalysts: dependence on Cu-Fe interaction, *ACS Sustain. Chem. Eng.* 6 (2018) 10182–10190.
- [34] Z.L. Li, W.L. Wu, M.L. Wang, Y.N. Wang, X.L. Ma, L. Luo, Y. Chen, K.Y. Fan, Y. Pan, H.L. Li, J. Zeng, Ambient-pressure hydrogenation of CO₂ into long-chain olefins, *Nat. Commun.* 13 (2022) 2396.
- [35] K. Nasriddinov, J.E. Min, H.G. Park, S.J. Han, J. Chen, K.W. Jun, S.K. Kim, Effect of Co, Cu, and Zn on FeAlK catalysts in CO₂ hydrogenation to C₅₊ hydrocarbons, *Catal. Sci. Technol.* 12 (2022) 906–915.
- [36] Q.Q. Xu, X.Q. Xu, G.L. Fan, L. Yang, F. Li, Unveiling the roles of Fe-Co interactions over ternary spinel-type ZnCo₂Fe₂-xO₄ catalysts for highly efficient CO₂ hydrogenation to produce light olefins, *J. Catal.* 400 (2021) 355–366.
- [37] M.K. Gnanamani, G. Jacobs, H.H. Hamdeh, W.D. Shafer, F. Liu, S.D. Hopps, G. A. Thomas, B.H. Davis, Hydrogenation of carbon dioxide over Co-Fe bimetallic catalysts, *ACS Catal.* 6 (2016) 913–927.
- [38] M. Rafati, L. Wang, A. Shahbazi, Effect of silica and alumina promoters on co-precipitated Fe-Cu-K based catalysts for the enhancement of CO₂ utilization during Fischer-Tropsch synthesis, *J. CO₂ Util.* 12 (2015) 34–42.
- [39] Y.H. Choi, E.C. Ra, E.H. Kim, K.Y. Kim, Y.J. Jang, K.N. Kang, S.H. Choi, J.H. Jang, J.S. Lee, Sodium-containing spinel zinc ferrite as a catalyst precursor for the selective synthesis of liquid hydrocarbon fuels, *ChemSusChem* 10 (2017) 4764–4770.
- [40] J.H. Liu, A.F. Zhang, X. Jiang, M. Liu, Y.W. Sun, C.S. Song, X.W. Guo, Selective CO₂ hydrogenation to hydrocarbons on Cu-promoted Fe-based catalysts: dependence on Cu-Fe interaction, *ACS Sustain. Chem. Eng.* 6 (2018) 10182–10190.
- [41] G. Kresse, J. Furthmüller, Efficiency of ab-initio total energy calculations for metals and semiconductors using a plane-wave basis set, *Comput. Mater. Sci.* 6 (1996) 15–50.
- [42] J.P. Perdew, J.A. Chevary, S.H. Vosko, K.A. Jackson, M.R. Pederson, D.J. Singh, C. Fiolhais, Atoms, molecules, solids, and surfaces-applications of the generalized gradient approximation for exchange and correlation, *Phys. Rev. B* 46 (1992) 6671–6687.
- [43] P.E. Blöchl, Projector augmented-wave method, *Phys. Rev. B* 50 (1994) 17953.
- [44] G. Henkelman, B.P. Uberuaga, H. Jonsson, A climbing image nudged elastic band method for finding saddle points and minimum energy paths, *J. Chem. Phys.* 113 (2000) 9901–9904.
- [45] S.Z. Li, A.W. Li, S. Krishnamoorthy, E. Iglesia, Effects of Zn, Cu, and K promoters on the structure and on the reduction, carburization, and catalytic behavior of iron-based fischer-tropsch synthesis catalysts, *Catal. Lett.* 77 (2001) 197–205.
- [46] P. Zhai, C. Xu, R. Gao, X. Liu, M.Z. Li, W.Z. Li, X.P. Fu, C.J. Jia, J.L. Xie, M. Zhao, X. P. Wang, Y.W. Li, Q.W. Zhang, X.D. Wen, D. Ma, Highly tunable selectivity for syngas-derived alkenes over zinc and sodium-modulated Fe₃C₂ catalyst, *Angew. Chem. Int. Ed.* 55 (2016) 9902–9907.
- [47] J. Wei, Q.J. Ge, R.W. Yao, Z.Y. Wen, C.Y. Fang, L.S. Guo, H.Y. Xu, J. Sun, Directly converting CO₂ into a gasoline fuel, *Nat. Commun.* 8 (2017) 15174.
- [48] C. Zhang, M.J. Xu, Z.X. Yang, M.H. Zhu, J. Gao, Y.F. Han, Uncovering the electronic effects of zinc on the structure of Fe₃C₂-ZnO catalysts for CO₂ hydrogenation to linear α -olefins, *Appl. Catal. B Environ.* 295 (2021), 120287.
- [49] Z.Q. Zhang, G.X. Huang, X.L. Tang, H.R. Yin, J.C. Kang, Q.H. Zhang, Y. Wang, Zn and Na promoted Fe catalysts for sustainable production of high-valued olefins by CO₂ hydrogenation, *Fuel* 309 (2022), 122105.

- [50] Q. Yang, V.A. Kondratenko, S.A. Petrov, D.E. Doronkin, E. Saraçi, H. Lund, A. Arinchein, R. Kraehnert, A.S. Skrypnik, A.A. Matvienko, E.V. Kondratenko, Identifying performance descriptors in CO₂ hydrogenation over iron-based catalysts promoted with alkali metals, *Angew. Chem. Int. Ed.* 61 (2022), e202116517.
- [51] C. Zhang, C.X. Cao, Y.L. Zhang, X.L. Liu, J. Xu, M.H. Zhu, W.F. Tu, Y.F. Han, Unraveling the role of zinc on bimetallic Fe₅C₂-ZnO catalysts for highly selective carbon dioxide hydrogenation to high carbon α -olefins, *ACS Catal.* 11 (2021) 2121–2133.
- [52] J. Zhu, P. Wang, X.B. Zhang, G.G. Zhang, R.T. Li, W.H. Li, T.P. Senftle, W. Liu, J. Y. Wang, Y.L. Wang, A.F. Zhang, Q. Fu, C.S. Song, X.W. Guo, Dynamic structural evolution of iron catalysts involving competitive oxidation and carburization during CO₂ hydrogenation, *Sci. Adv.* 8 (2022) eabm3629.
- [53] L.S. Guo, J. Sun, X.W. Ji, J. Wei, Z.Y. Wen, R.W. Yao, H.Y. Xu, Q.J. Ge, Directly converting carbon dioxide to linear α -olefins on bio-promoted catalysts, *Commun. Chem.* 1 (2018) 11.
- [54] Z.P. Zhang, J. Zhang, X. Wang, R. Si, J. Xu, Y.F. Han, Promotional effects of multiwalled carbon nanotubes on iron catalysts for Fischer-Tropsch to olefins, *J. Catal.* 365 (2018) 71–85.